TUM

Technische Universität München

Data-Driven Design of Platinum Electrocatalysts for Efficient Oxygen Reduction

Marlon Rück, M.Sc.

Vollständiger Abdruck der von der Fakultät für Elektrotechnik und Informationstechnik der Technischen Universität München zur Erlangung des akademischen Grades eines

Doktor-Ingenieurs (Dr.-Ing.)

genehmigten Dissertation.

Vorsitzender: Prof. Dr. Rolf Witzmann

Prüfer der Dissertation: 1.   Prof. Dr. Alessio Gagliardi

2.   Prof. Aldo di Carlo, Ph.D.

3.   Prof. Dr. Aliaksandr S. Bandarenka

Die Dissertation wurde am 15.04.2020 bei der Technischen Universität München eingereicht und durch die Fakultät für Elektrotechnik und Informationstechnik am 01.09.2020 angenommen.

Acknowledgements

I express my deepest gratitude to my PhD supervisor Alessio Gagliardi for his great support to thrive on my scientific work at TUM. I appreciate the exciting opportunities he gave me in developing our research program, working with collaborators on interdisciplinary projects, and building global networks by presenting research outcomes on various worldwide conferences. This has opened the creative space to develop innovative ideas and effective novel approaches.

I am very grateful to my PhD mentor Markus Becherer for his exceptional support to my professional success at TUM. I am thankful for his effort in making and maintaining the whole chair of Nanoelectronics a fantastic working environment.

I like to show my greatest thanks to Aliaksandr Bandarenka for using his great expertise in catalysis to drive our fruitful collaborations on diverse projects.

Likewise, I am really grateful to Federico Calle-Vallejo for boosting the success of our joint projects through his deep know-how in catalyst modeling and exceptional written communication skills.

I whole-heartedly appreciate working with Batyr Garlyyev and Kathrin Kratzl. I am grateful for our joint achievements in transforming catalyst development from computational design into catalyst synthesis and characterization.

I am very thankful to all my great colleagues and friends from our SNE research group, that are Tim, Manuel, Suyan, Felix, Mohammed, Waldemar, Fred, Ajay, Michael, Obaidur, and Kashif, and the whole Nanoelectronics chair. It is amazing working with you, sharing ideas and knowledge, and enjoying International Conferences of Mostly Scientific Topics (ICMST) and much more.

I wish to extend my cordial thanks to Aldo di Carlo for sharing his expertise and continuative ideas for future studies.

I owe a very important debt to the awesome members of Stanford's SunCat for hosting the amazing Summer Institute 2019, which enabled me to engage with so many fascinating people striving for sustainable energy technologies around the world.

Publications in
International Peer-Reviewed Journals

Core Publication I:
M. Rück, A. Bandarenka, F. Calle-Vallejo, A. Gagliardi, "Oxygen Reduction Reaction: Rapid Prediction of Mass Activity of Unstrained Nanostructured Platinum Electrocatalysts," *J. Phys. Chem. Lett.*, 2018, 9 (15), 4463-4468.
DOI:10.1021/acs.jpclett.8b01864

B. Garlyyev[1], K. Kratzl[1], M. Rück[1], J. Michalička, J. Fichtner, J. Macak, T. Kratky, S. Günther, M. Cokoja, A.S. Bandarenka, A. Gagliardi, R.A. Fischer, "Optimizing the Size of Platinum Nanoparticles for Enhanced Oxygen Electro-Reduction Mass Activity," *Angew. Chem. Int. Ed.*, 2019, 58 (28), 9596-9600.
DOI:10.1002/anie.201904492
[1] First authors

Core Publication II:
M. Rück, A. Bandarenka, F. Calle-Vallejo, A. Gagliardi, "Fast Identification of Optimal Pure Platinum Nanoparticle Shapes and Sizes for Efficient Oxygen Electroreduction," *Nanoscale Adv.*, 2019, 1 (8), 2901–2909.
DOI:10.1039/c9na00252a

M. Rück, B. Garlyyev, F. Mayr, A.S. Bandarenka, A. Gagliardi, "Oxygen Reduction Activities of Strained Platinum Core–Shell Electrocatalysts Predicted by Machine Learning," *J. Phys. Chem. Lett.*, 2020, 11 (5), 1773-1780.
DOI:10.1021/acs.jpclett.0c00214

Related Academic Press Releases

"Activity of Fuel Cell Catalysts Doubled", TUM Corporate Communications Center, July 03, 2019. `https://www.tum.de/nc/en/about-tum/news/press-releases/details/35554/`

"Machine Learning for Improved Fuel Cell Catalysts", Cluster of Excellence *e*-conversion, May 01, 2020. `https://www.e-conversion.de/machine-learning-for-improved-fuel-cell-catalysts/`

"Fuel Cell Research", Cluster of Excellence *e*-conversion, June 06, 2020. `https://www.e-conversion.de/fuel-cell-research/`

International Conference Contributions

M. Rück, A. Gagliardi, "Rapid Computation of Mass Activities of Nanostructured Platinum Electrocatalysts for the Oxygen Reduction Reaction," Designing Nanoparticle Systems for Catalysis: Faraday Discussions, London UK, 16-18 May, 2018, *Poster Presentation.* DOI:10.1039/c8fd90018c

M. Rück, A. Gagliardi, "Nanostructuring Pure Platinum Shapes and Sizes for Efficient Oxygen Electroreduction," Materials Research Society (MRS) Fall Meeting, Boston MA USA, 25-30 Nov, 2018, *Poster Presentation.*

M. Rück, A. Gagliardi, "Optimized Platinum Electrocatalyst Designs for Efficient Oxygen Reduction," EuropaCat, Aachen Germany, 18-23 Aug, 2019, *Poster Presentation.*

M. Rück, A. Gagliardi, "Tailoring Shapes and Sizes of Pure Pt Electrocatalysts to Improve the Oxygen Reduction Activity," 236th ECS Meeting, Atlanta GA USA, 13-17 Oct, 2019, *Oral Presentation.* DOI:10.1149/ma2019-02/35/1531

International Summer School Contribution

M. Rück, A. Gagliardi, "Data-Driven Electrocatalyst Designs for Efficient Oxygen Reduction," SunCat Summer Institute, Stanford CA USA, 12-16 Aug, 2019, *Poster Presentation.*

Abstract

Electrocatalysis technologies including proton-exchange membrane (PEM) fuel cells can help shape the sustainable energy future, in which PEM fuel cells provide versatile stationary and portable power solutions. However, one key factor limiting their widespread commercialization are high costs for large Platinum (Pt) loadings, which are required to catalyze the sluggish oxygen reduction reaction (ORR) at the fuel cell cathode. Thus, it is of great interest to enhance the catalyst activity with respect to the Pt mass.

In this thesis, we capitalize on data-driven design to propose new Pt catalysts with enhanced mass activities toward the ORR. We link experimental data with results from density functional theory (DFT) on Pt-based ORR catalysts to build a computational model, which predicts mass activities in good agreement with experiments. Beyond thitherto available experiments, highest mass activities are predicted for pure Pt nanoparticles with 1, 2, and 3 nm size.

In interdisciplinary collaborations, we accomplished synthesis of the proposed 1 nm sized pure Pt nanoparticles using a metal-organic framework. The measured mass activities of 0.87 ± 0.14 A mg_{Pt}^{-1} coincide with the computational predictions (0.99 A mg_{Pt}^{-1}) and double the mass activity of current commercial Pt/C electrocatalysts.

The herein observed theoretical limit, that pure Pt nanoparticles with sphere-like shapes are limited to ca 2 A mg_{Pt}^{-1} in mass activity, substantiates the high demand for shape and size engineering toward further enhanced mass activities. We present a computational framework for high-throughput screenings to tailor electrocatalyst shapes and sizes toward optimized mass activities. The tailored electrocatalysts show high predicted mass activities of up to 4.28 A mg_{Pt}^{-1}, which corresponds to 7.8-fold enhancement over Tanaka commercial Pt/C catalysts. The high activities originate from numerous active sites, which are arranged in a side-by-side formation at concave kinks of the nanostructure.

In core-shell nanoparticles, the catalysis is driven on active Pt shells, but cheaper and more abundant metals at the core limit the precious Pt loading. We present a machine learning framework for strain prediction on core-shell nanoparticles. Machine learning predictions are linked with the aforementioned computational model to forecast mass activities of core-shell nanoparticles. We show that optimal strain degrees, which enhance mass activities, depend on the nanoparticle size. Large compressive strains on Pt@Cu and Pt@Ni result in optimal mass activities of up to 2.2 A mg_{Pt}^{-1} at 1.94 nm nanoparticle size. Weaker compressive strains on Pt@Ag and Pt@Au induce similar high mass activities at 2.83 nm. Thus, we propose core-shell nanoparticles with various metal compositions, which are up to 4 times more active than commercial Pt/C electrocatalysts.

Zusammenfassung

Elektrokatalyse-Technologien, einschließlich Protonenaustauschmembran-Brennstoff-zellen (PEM-Brennstoffzellen), können maßgeblich zur nachhaltigen Energiezukunft beitragen. PEM-Brennstoffzellen bieten hierfür vielseitige stationäre und mobile Stromversorgungslösungen. Ein Schlüsselfaktor, der deren weit verbreitete Kommerzialisierung einschränkt, sind die hohen Kosten für große Mengen Platin (Pt), welche für die Katalyse der Sauerstoffreduktion (ORR) an der Brennstoffzellenkathode benötigt werden. Daher ist es von großem Interesse, die Katalysatoraktivität relativ zur benötigten Pt-Menge zu verbessern.

In dieser Arbeit nutzen wir datenbasiertes Design, um neue Pt-Katalysatoren mit verbesserten Massenaktivitäten für die ORR zu entwickeln. Wir verknüpfen experimentelle Daten mit Ergebnissen der Dichtefunktionaltheorie (DFT) für Pt-Katalysatoren der ORR, um ein Computermodell zu erstellen, das Massenaktivitäten in guter Übereinstimmung mit Experimenten vorhersagt. Über die bis dahin verfügbaren Experimente hinaus werden für reine Pt-Nanopartikel mit einer Größe von 1, 2 und 3 nm die höchsten Massenaktivitäten prognostiziert.

In interdisziplinären Kooperationen haben wir die Synthese der vorgeschlagenen Pt-Nanopartikel mit einer Größe von 1 nm unter Verwendung eines metallorganischen Gerüsts (MOF) durchgeführt. Die gemessenen Massenaktivitäten von $0{,}87 \pm 0{,}14$ A mg_{Pt}^{-1} stimmen mit der computergestützten Prognose ($0{,}99$ A mg_{Pt}^{-1}) überein und verdoppeln die Massenaktivität von derzeitigen kommerziellen Pt/C-Elektrokatalysatoren.

Das hier beobachtete theoretische Limit, dass reine Pt-Nanopartikel mit sphärischer Form eine Massenaktivität von maximal ca. 2 A mg_{Pt}^{-1} aufweisen, untermauert die hohe Nachfrage nach Katalysatoren mit maßgeschneiderten Formen und Größen, die weiter verbesserte Massenaktivitäten aufweisen. Wir präsentieren ein computergestütztes Modell für Hochdurchsatz-Screenings, um die Formen und Größen von Elektrokatalysatoren hin zu bestmöglichen Massenaktivitäten zu optimieren. Die maßgeschneiderten Elektrokatalysatoren weisen hohe prognostizierte Massenaktivitäten von bis zu $4{,}28$ A mg_{Pt}^{-1} auf, was einer 7,8-fachen Verbesserung gegenüber derzeitigen kommerziellen Pt/C-Katalysatoren von Tanaka entspricht. Die hohen Aktivitäten sind auf zahlreiche aktive Zentren zurückzuführen, die an konkaven Einbuchtungen der Nanostruktur nebeneinander angeordnet sind. In Kern-Schale-Nanopartikeln geschieht die Katalyse auf aktiven Pt-Schalen, wobei der Kern aus wirtschaftlich günstigeren und häufiger vorkommenden Metallen besteht, um den kostspieligen Pt-Anteil zu beschränken. Wir konstruieren Modelle des maschinellen Lernens zur Prognose von atomaren Dehnungen und Kompressionen in Kern-Schale-Nanopartikeln.

Die Prognosen des maschinellen Lernens werden mit dem oben genannten Com-

putermodell verknüpft, um Massenaktivitäten von Kern-Schale-Nanopartikeln vorherzusagen. Wir zeigen, dass optimale Dehnungs- oder Kompressionsgrade, welche die Massenaktivitäten verbessern, von der Nanopartikelgröße abhängen. Starke Kompressionen in Pt@Cu und Pt@Ni führen zu optimalen Massenaktivitäten von bis zu 2,2 A mg$_{Pt}^{-1}$ bei einer Nanopartikelgröße von 1,94 nm. Die schwächeren Kompressionen in Pt@Ag und Pt@Au induzieren ähnlich hohe Massenaktivitäten bei 2,83 nm. Die vorgeschlagenen Kern-Schale-Nanopartikel mit verschiedenen Metallzusammensetzungen sind somit bis zu viermal aktiver als derzeitige kommerzielle Pt/C-Elektrokatalysatoren.

Contents

1 Introduction

This thesis is a publication-based dissertation, which therefore stands as complement to the overall scientific outcome from the articles already published in international scientific journals. The Introduction expounds the motivation of the work in context with previous scientific contributions on electrochemical technologies for a sustainable energy future. The Methods section provides concepts and tools, which have been developed and applied on solving the scientific challenges. Article summaries and a cross-article discussion explicate how the combined results from this work have been contributing to scientific progress in the associated research field.

Electrocatalytic technologies attract unprecedented attention to transform the energy landscape in power supply, chemical and manufacturing industries, and transportation.[1] Using electricity from renewable sources, emerging Power-To-X technologies catalyze pervasive resources into valuable feedstocks, which can substitute their production from fossil fuels (see Figure 1.1). For instance, electrocatalysts drive the reduction of CO_2 to feedstocks like CO, methanol, and hydrocarbons.[2–12] Water electrolyzers produce H_2 and O_2 by hydrogen (HER) and oxygen evolution reactions (OER)[13–16] as a clean alternative to methane steam reforming.[17] Catalyzed hydrocarbons are important feedstocks in plastics production or synthetic fuels for combustion engines.[18–20] Syngas composed of hydrogen, carbon monoxide, and carbon dioxide is inevitable for a variety of chemical processes including industrial synthesis of methanol. Hydrogen allows carbon-free reduction of iron oxides in iron and steel production, which makes up some percent of the direct global CO_2 emissions from fossil fuels.[21] Combining water electrolyzers with proton exchange-membrane (PEM) fuel cells can bridge the gap between excesses and shortages in renewable power supply: Water electrolyzers compensate power excesses by H_2 and O_2 production. PEM fuel cells reconvert stored hydrogen[22] to electricity by anodic hydrogen oxidation and cathodic oxygen reduction reaction (ORR).

However, widespread commercialization of water electrolyzers and PEM fuel cells are hindered by high costs and scarcity of precious metals, which catalyze the sluggish kinetics of OER and ORR.[13,23] In CO_2 electroreduction, limited Faradaic efficiencies impair the selectivities of catalyzed feedstocks.[20,24–26] Thus, new catalysts fitted to chemistry can enhance activities and selectivities to drive the sustainable energy future.[1] In this thesis, tailoring Pt catalysts by data-driven design is the strategy pursued to translate ORR requirements into catalyst design solutions.
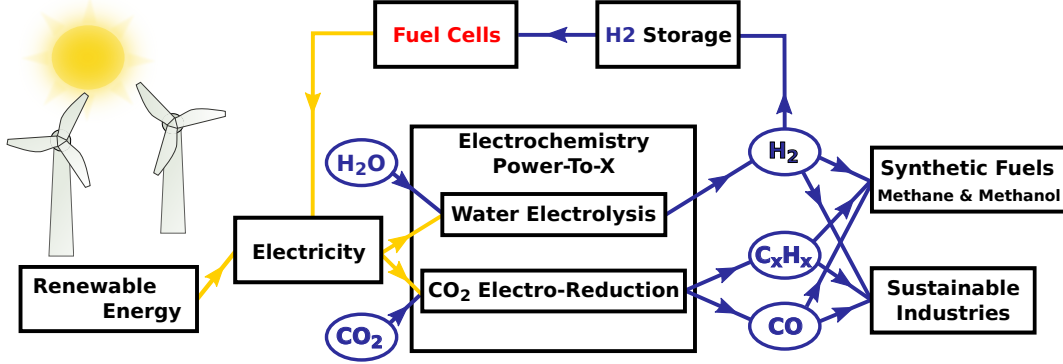
Figure 1.1: Sustainable energy future

Like in PEM fuel cells, hydrogen is the energy carrier in several types of fuel cells such as alkaline fuel cells, solid oxide fuel cells, molten carbonate fuel cells, and phosphoric acid fuel cells.[27] Their diversity in operating temperatures and electrolyte/membrane material properties provides widespread stationary and portable power applications. PEM fuel cells stand out in power density, compact structure, and their large application range.[28]

At the anode side of PEM fuel cells, hydrogen is oxidized into protons and electrons (see Figure 1.2) given by

$$2H_2(g) \rightarrow 4H^+ + 4e^- \ , \tag{1.1}$$
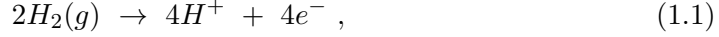
for which currently Pt is the prevalent catalyst. By definition, hydrogen oxidation has zero standard potential versus the reversible hydrogen electrode (RHE). The ionomer in the PEM conducts protons from anode to cathode. Electrons take the path from anode across the consumer load to the cathode. The ORR at the cathode converts protons, electrons, and oxygen into water,

$$O_2(g) + 4H^+ + 4e^- \rightarrow 2H_2O(l) \ , \tag{1.2}$$
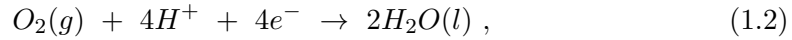
at 1.23 V standard potential versus RHE. Therefore, the two half-reactions result in the overall PEM fuel cell reaction

$$O_2(g) + 2H_2(g) \rightarrow 2H_2O \tag{1.3}$$
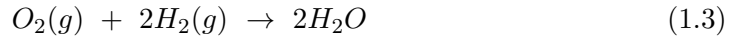
at 1.23 V standard potential.

Since the four-electron transfer ORR is many times slower than hydrogen oxidation reaction with two-electron transfers, the ORR limits the fuel cell performance.[29,30] Besides cell durability,[31,32] increasing the ORR performance is therefore the major challenge toward viable economic commercialization of PEM fuel cells.
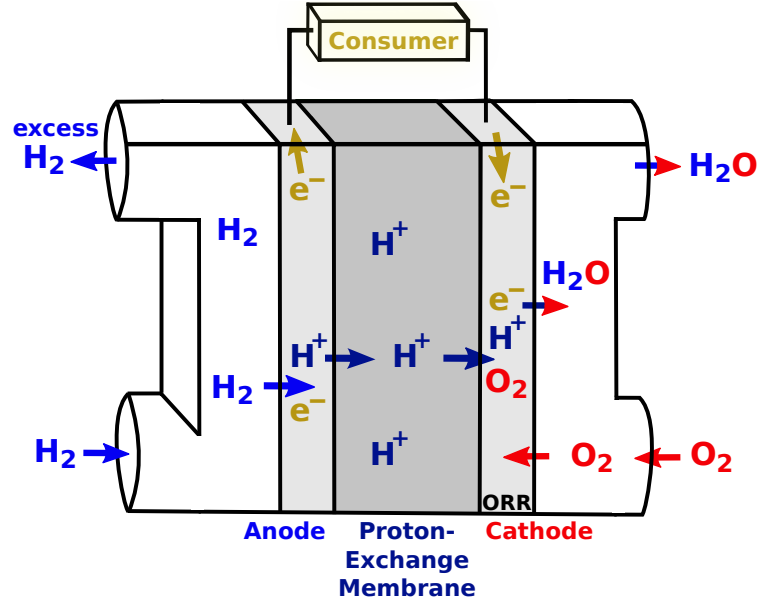
Figure 1.2: Proton-exchange membrane (PEM) fuel cell

More specifically, only Pt-based electrocatalysts have shown appropriate ORR activity and stability.[1,33] Regarding high costs and scarcity of Pt, it is decisive to enhance the catalyst activity with respect to the Pt mass. The US Department of Energy (DOE) has defined the mass activity target for 2020 at 0.44 A/mg_{PMG}, which is given in terms of the platinum group metal mass mg_{PMG} in PEM fuel cells at 0.9 V cell potential.[34,35] At cell potentials below 0.9 V, high power densities of 0.125 mg_{PMG}/W are the US DOE's target.[34,35]
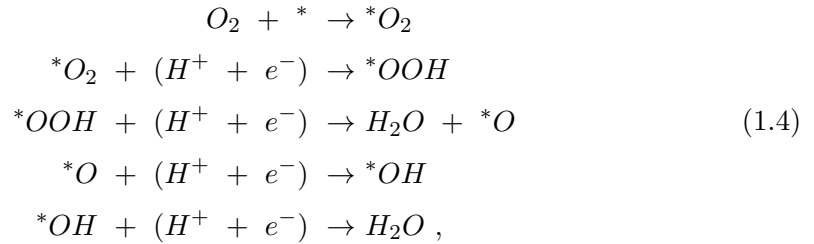
It has been proposed that the four-electron transfer ORR is catalyzed via hydroxyl and peroxyl intermediates in the elementary steps[36]

$$
\begin{aligned}
O_2 \ + \ ^* &\rightarrow \ ^*O_2 \\
^*O_2 \ + \ (H^+ \ + \ e^-) &\rightarrow \ ^*OOH \\
^*OOH \ + \ (H^+ \ + \ e^-) &\rightarrow H_2O \ + \ ^*O \\
^*O \ + \ (H^+ \ + \ e^-) &\rightarrow \ ^*OH \\
^*OH \ + \ (H^+ \ + \ e^-) &\rightarrow H_2O \ ,
\end{aligned}
\tag{1.4}
$$

where * denotes species adsorbed on the catalyst surface. With regard to Sabatier's principle, the ORR activity is chiefly controlled by adsorption energies of the reaction intermediates.[36–38] More precisely, numerous experimental studies on pure Pt and Pt-alloy electrocatalysts revealed that weakening the $^*OH$ adsorption energies by 0.1-0.15 eV relative to Pt(111) leads to enhanced catalytic activities.[39–43]

Adsorption energies of reaction intermediates are sensitively controlled not only by

the catalyst material, but also by the electrolyte,[44] catalyst nanostructure,[41,43,45–48] and the type of carbon support.[49] Pt high-index planes have active sites near surface steps,[50] which enhance the activity over Pt(111).[51–54] Meso-structured Pt thin-films have shown improved activities at similar stabilities compared to ETEK commercial Pt/C catalysts.[55] On Pt nanoparticles, highest activities have been oberserved for nanoparticle sizes around 3 nm.[40,56–58]

In the last decade, record mass activities have been reported on nanostructured Pt-alloy electrocatalysts.[33,59,60] Low index surfaces $Pt_3Ni(111)$, $Pt_3Ni(100)$, and $Pt_3Ni(110)$ have highly improved activities relative to their Pt(111), Pt(100), and Pt(110) equivalents.[61] This stimulated seminal studies on PtNi octahedra[62,63] and PtNi nanoframes,[64] which demonstrate superior mass activities relative to commercial Pt/C catalysts. Surface dopants of Rh,[65] Mo,[66] and Ga[67] increase the stability of PtNi octahedra.

Designing nanocatalysts with optimal adsorption energies is increasingly addressed by linking theory with experiments.[1,43,68] Geometric descriptors, such as generalized coordination numbers,[43,50,69] establish the relation between catalyst morphologies and adsorption energies. For a site i, the generalized coordination number

$$\overline{CN}(i) = \sum_{j=1}^{n_i} \frac{cn(j)}{cn_{max}} \qquad (1.5)$$

sums up the coordination $cn(j)$ of the n_i nearest neighbors j. The sum over nearest neighbors is normalized by the bulk atom coordination cn_{max}, which is $cn_{max} = 12$ in the fcc lattice of Pt. Therefore, $\overline{CN}$ determines finite size effects and local site structures up to second nearest neighbors around the active sites. Density functional theory (DFT) calculations have revealed that $\overline{CN}$ is linearly related to adsorption energies of all crucial ORR intermediates $^*O_2$, $^*O$, $^*OH$, $^*OOH$, $^*H_2O$, and $^*H_2O_2$ on Pt.[43,69] Generalized coordination numbers also capture strain effects on strained Pt sites, where adsorption energies approximately follow the same coordination trends as on unstrained Pt catalysts.[70,71] A Sabatier analysis, which takes DFT adsorption energies versus $\overline{CN}$ into account, shows that sites with $7.5 < \overline{CN} \leq 8.3$ boost the activity over Pt(111).[43,50] Single sites with high activities over Pt(111) have been proposed in concave kinks[43] and tailored nanostructures.[50] How high ratios of active sites can be incorporated in stable nanostructures is the overall challenge addressed in this thesis.

Linear descriptors including d-band centers,[72–74] extended coordination numbers,[71,75,76] and binding energies,[77,78] have recently aided in the search for active bimetallic ORR catalysts. In core-shell nanoparticles, the core can be made of more abundant metals than Pt, but the catalysis is driven on active Pt shells.[41,79,80] The lattice mismatch between core and shell may induce strain and/or ligand effects shift-

ing adsorption energies of intermediates,[42,81–83] which are predominantly controlled by nanoparticle size, core material, and shell thickness.[41,77,80,84–88] Ligand effects drop rapidly with shell thickness and vanish from the 3rd atomic layer.[41,89–91] Strain effects start decreasing slowly from the 5th atomic layer instead.[41,89,91] This has been experimentally observed on Pt@Cu[84] and Pt@Y[85] core-shell nanoparticles with Pt shell thicknesses of 0.6-1.0 nm and 0.7-1.3 nm, respectively. The high mass activities are rationalized by strain rather than ligand effects.[39,84,85,92] Similar high mass activites as on Pt@Y have been reported on Ti-Au@Pt, where the bimetallic Ti-Au core increases the stability relative to Au@Pt.[80]
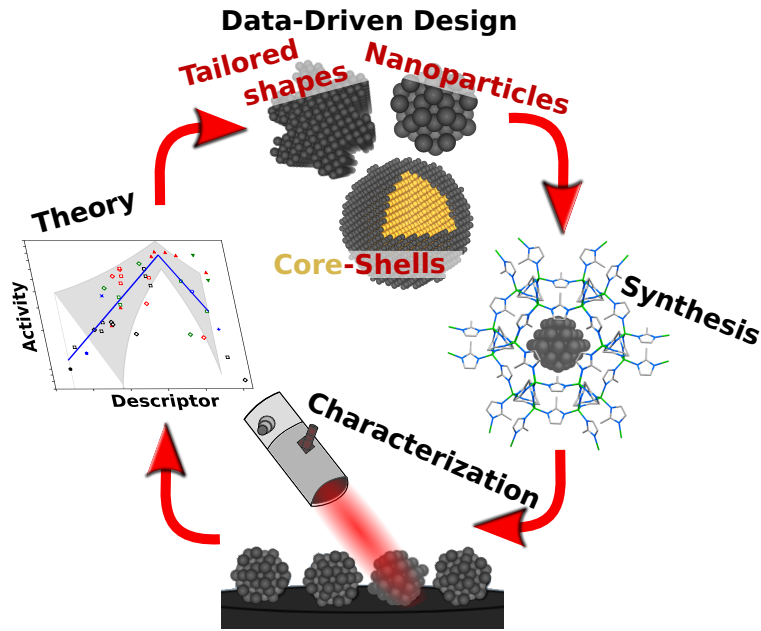
Figure 1.3: Data-driven design of Pt-based electrocatalysts. Predictive theory proposes optimized catalyst designs for synthesis. Synthesized catalysts are characterized experimentally. Experimental insights improve the predictive theory.

In this thesis, we propose new catalysts by data-driven design (see Figure 1.3), which show enhanced mass activities toward the ORR. We first present a computational model, which is based on coordination-activity relations, to predict ORR activities of Pt catalysts within short computation times. We apply the computational model on Pt nanoparticles, for which we identify optimal activities near 1, 2, and 3 nm in size toward smallest size distribution. The computationally proposed 1 nm sized nanoparticles are synthesized in a metal organic framework.

Furthermore, we tailor nanocatalyst shapes toward highest activity using activity predictions from our computational model. Stability criteria are taken into account. Tailored nanocatalyst shapes are created by the Superformula, which yields a variety of nanoshapes depending on numerical parameters.

To investigate core-shell nanoparticles, we propose a machine learning approach for strain prediction, which facilitates screening the vast core-shell design space. Based

on machine learning predictions of strain, we apply the computational model to forecast mass activities of core-shell nanoparticles. Nanoparticle sizes, which yield optimal mass activities, are proposed for Pt shells on various core metals. Furthermore, we rationalize how strain effects can enhance ORR activities.

2 Methods

2.1 Strained generalized coordination numbers

Compressive and tensile strain effectively increase and decrease the coordination around one atom. This effect is described by the strained coordination[70]

$$cn^*(j) = \sum_{k=1}^{cn(j)} \frac{a_{nn}(j)}{|\boldsymbol{r}_j - \boldsymbol{r}_k|} \ ,$$

(2.1)

which weights the bulk interatomic distance $a_{nn}(j)$ with respect to the distance between atomic positions $\boldsymbol{r}_j$ of atom j and atoms k for all nearest neighbors, which are $cn(j)$ in total. Therefore, the strained coordination can be interpreted as weighted nearest neighbor counting. The bulk interatomic distances are given by

$$a_{nn}(j) \approx \begin{cases} 0.2892 \ nm & , \text{if } j \text{ is Ag atom} \\ 0.2885 \ nm & , \text{if } j \text{ is Au atom} \\ 0.2772 \ nm & , \text{if } j \text{ is Pt atom} \\ 0.2751 \ nm & , \text{if } j \text{ is Pd atom} \\ 0.2553 \ nm & , \text{if } j \text{ is Cu atom} \\ 0.2489 \ nm & , \text{if } j \text{ is Ni atom} . \end{cases}$$

(2.2)

The strained coordination determines site-specific strain[70]

$$1 - \frac{cn^*(j)}{cn(j)}$$

(2.3)

for any site j. Mean strain

$$\frac{1}{N_{tot}} \sum_{j=1}^{N_{tot}} \left[1 - \frac{cn^*(j)}{cn(j)} \right] \ ,$$

(2.4)

is the average site-specific strain over all N_{tot} atoms of the nanoparticle. Similar to $\overline{CN}$ in Eq. 1.5, the sum over strained coordinations determines the strained generalized coordination number

$$\overline{CN}^*(i) = \frac{1}{cn_{max}} \sum_{j=1}^{cn(i)} cn^*(j) \ .$$

(2.5)

On unstrained Pt catalysts, the interatomic distances reduce to the bulk nearest neighbor distance $|\boldsymbol{r}_j - \boldsymbol{r}_k| = a_{nn}(j)$, so that cn^* and $\overline{CN}^*$ are described by their

unstrained equivalents[70]

$$cn^*(j)\big|_{||\boldsymbol{r}_j - \boldsymbol{r}_k|=a_{nn}(j)} = cn(j) \tag{2.6}$$

and

$$\overline{CN}^*(i)\big|_{||\boldsymbol{r}_j - \boldsymbol{r}_k|=a_{nn}(j)} = \overline{CN}(i) = \frac{1}{cn_{max}} \sum_{j=1}^{cn(i)} cn(j) \ . \tag{2.7}$$

On extended surfaces, the coordination cn describes adsorption energies appropriately.[93,94] However, adsorption energies on nanoparticles remain out of scope because of finite size effects.[95,96] In contrast, $\overline{CN}$ captures local site structures up to the second nearest neighbor sphere around active sites, so that $\overline{CN}$ describe adsorption energies on various unstrained[8,43,50,69,97–100] and strained[70,71] extended surfaces and nanoparticles. It is important to note that adsorption energies of *OH and *OOH on strained Pt sites follow approximately the same trend in $\overline{CN}^*$ as on unstrained Pt sites.[70]

In Figure 2.1, the determination of $\overline{CN}$ is exemplified for one selected site. The selected site (highlighted in yellow) has ten nearest neighbors with coordination 6, 7, 9, or 12. Therefore, the selected site has

$$\overline{CN} = \sum_{j=1}^{10} \frac{cn(j)}{12} = \frac{2 \times 6 + 7 + 2 \times 9 + 5 \times 12}{12} = 8.08 \ . \tag{2.8}$$

Since local site structures with $7.5 < \overline{CN} \leq 8.3$ have enhanced activity over Pt(111),[43,50] the selected site is active for the ORR.
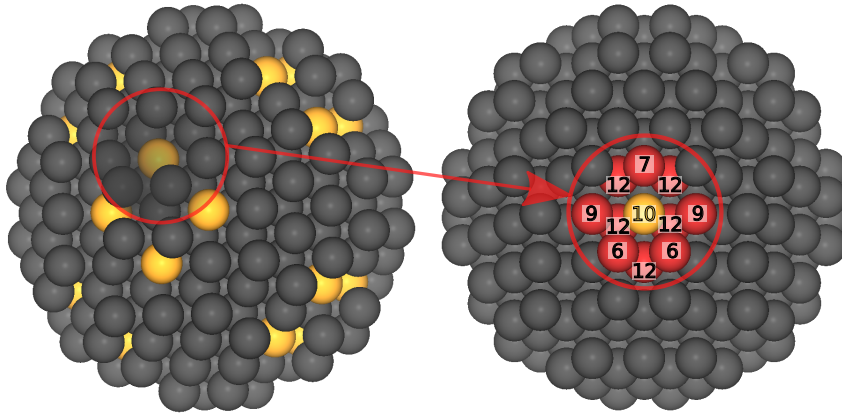
Figure 2.1: Determination of $\overline{CN}$ on nanoparticles. The selected site (highlighted in yellow and enclosed by red circle) has 10 nearest neighbor sites (colored in red). Numbers indicate the atomic coordination. Adapted with permission from Ref. 101. Copyright 2019 Wiley.
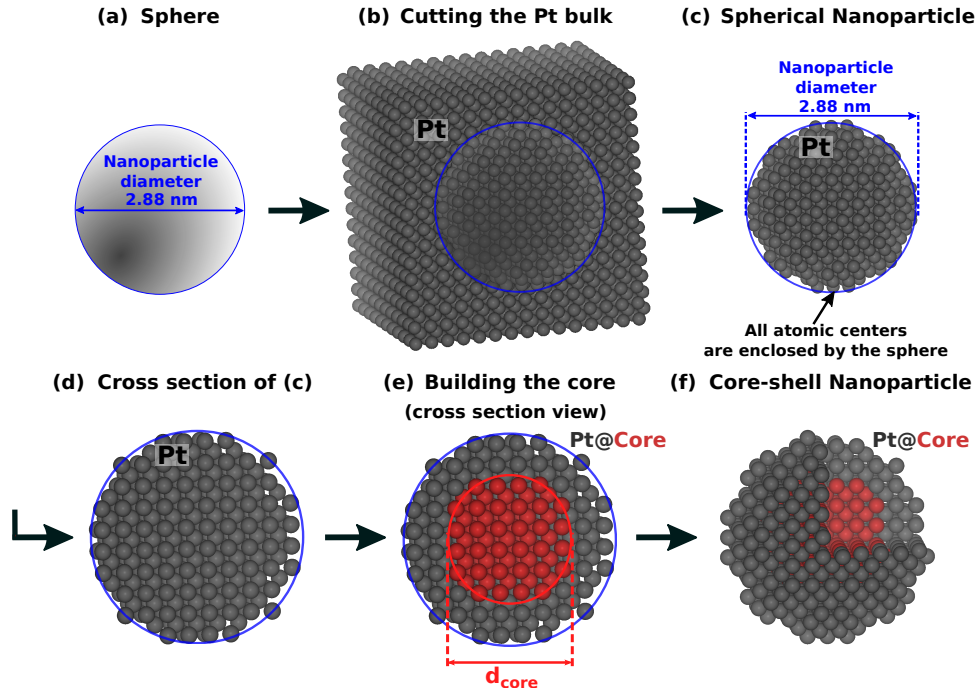
2.2 Generation of Pure Platinum and Platinum Core-Shell Nanoparticles

The generation of spherical nanoparticles, which are used for computational activity predictions, is illustrated in Figure 2.2. A sphere is created for each nanoparticles, where the diameter of the sphere corresponds to the nanoparticle diameter. The shape of the sphere is cut out from the fcc Pt bulk. All atoms, whose atomic centers are enclosed by the sphere, belong to the nanoparticle. Therefore, upon very small changes in the diameter of the sphere, the resulting nanoparticle may be identical. For instance, diameters of 2.87 nm and 2.88 nm result in the same nanoparticle. A larger diameter of 2.89 nm generates a different nanoparticle instead.

In core-shell nanoparticles, the core contains all atoms within radius $d_{core}/2$ around the nanoparticle center (see Figure 2.2e). The definition

$$d_{core} = 2 \left[\max(r_i) - a_{nn}^{Pt}(n_{layer} - 0.02) \right] \tag{2.9}$$

yields 2-3 monolayer Pt shells for $n_{layer} = 2$ and 3-4 monolayer Pt shells for $n_{layer} = 3$. Given that r_i is the distance between atom i and the nanoparticle center, $\max(r_i)$ is the nanoparticle size with respect to the atom farthest away from the nanoparticle center. The Pt bulk interatomic distance reads $a_{nn}^{Pt} \approx 0.2772$ in Eq. 2.2.

(a) Sphere   **(b) Cutting the Pt bulk**   **(c) Spherical Nanoparticle**

(d) Cross section of (c)   **(e) Building the core (cross section view)**   **(f) Core-shell Nanoparticle**

Figure 2.2: Generation of pure Pt nanoparticles (a)-(c) and Pt core-shell nanoparticles (a)-(f) with cores of fcc metals Ag, Au, Pd, Cu, or Ni. Adapted with permission from Ref. 102. Copyright 2020 American Chemical Society.

## 2.3   Computational Model for Mass Activity Prediction

This concept is published and reproduced in part with permission from Ref. 103, J. Phys. Chem. Lett., 2018, 9 (15), 4463–4468. Copyright 2018 American Chemical Society.

Progress in the search for promising new catalysts is limited by costly synthesis on the experimental side and expensive computational approaches solely based on density functional theory (DFT) on the theory side.[104] In this section, we combine theoretical and experimental results to derive a computational model, which calculates ORR activities on Pt electrocatalysts within short computation times.

Previous experiments on extended Pt surfaces and Pt alloys have shown that weakening the *OH adsorption energy by $\sim$ 0.1-0.15 eV with respect to Pt(111) results in up to 8-fold enhanced activities.[41] Experimentally, *OH adsorption energies are determined by integrated cyclic voltammograms.[41,43]

Furthermore, on the atomic scale, *OH adsorption energies are linearly related with $\overline{CN}$.[43,69] The evaluation of $\overline{CN}$ and DFT-derived *OH adsorption energies (relative to OH in gas phase) on various sites reveals their linear relation

$$\Delta E_{OH} = 0.1916\,\overline{CN} - 3.8673 \tag{2.10}$$
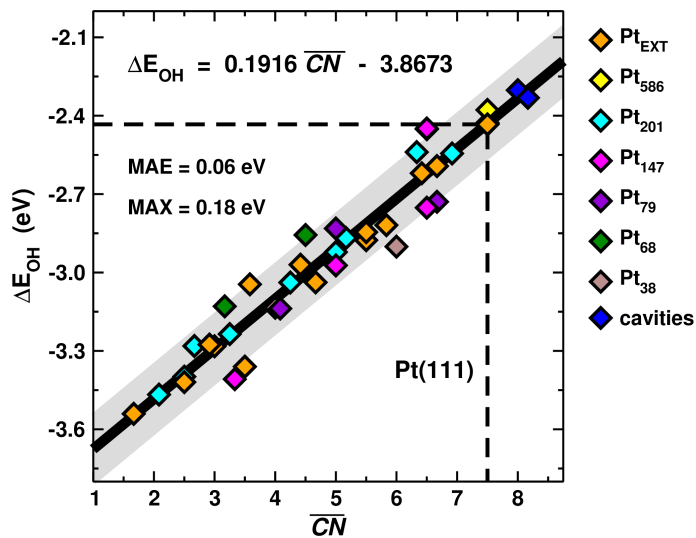
Figure 2.3: DFT-derived *OH adsorption energies (relative to OH in gas phase) versus $\overline{CN}$ on diversely coordinated sites at various catalyst shapes and sizes; including tetrahedrons (green), cuboctahedrons (magenta), truncated octahedrons (yellow, cyan, purple, brown), extended surfaces (orange), and cavities (blue). The adsorption energy dependence on $\overline{CN}$ is described by the linear function provided in the inset. The gray area covers $\pm$2MAE around the linear fit, which contains 75% of the calculated data points. Adapted with permission from Ref. 103. Copyright 2018 American Chemical Society.

in Figure 2.3.

In addition, experimentally measured activities versus *OH adsorption energies, which are given relatively to Pt(111), are provided from literature and presented in Figure 2.4. Using the linear relation in Eq. 2.10, we map the experimental *OH adsorption energies from Figure 2.4a onto site-specific

$$\overline{CN} = \frac{\Delta E_{OH} - \Delta E_{OH}^{Pt(111)}}{0.1916} + \overline{CN}_{Pt(111)} \tag{2.11}$$

in Figure 2.4b, where $\overline{CN}_{Pt(111)} = 7.5$ renormalizes the scale appropriately. The volcano-shaped activity trend

$$A_{volc}(\overline{CN}) = \begin{cases} A_1(\overline{CN}), & \text{if } \overline{CN} \leq \overline{CN}_{peak} \\ A_2(\overline{CN}), & \text{if } \overline{CN} > \overline{CN}_{peak} \end{cases} \tag{2.12}$$
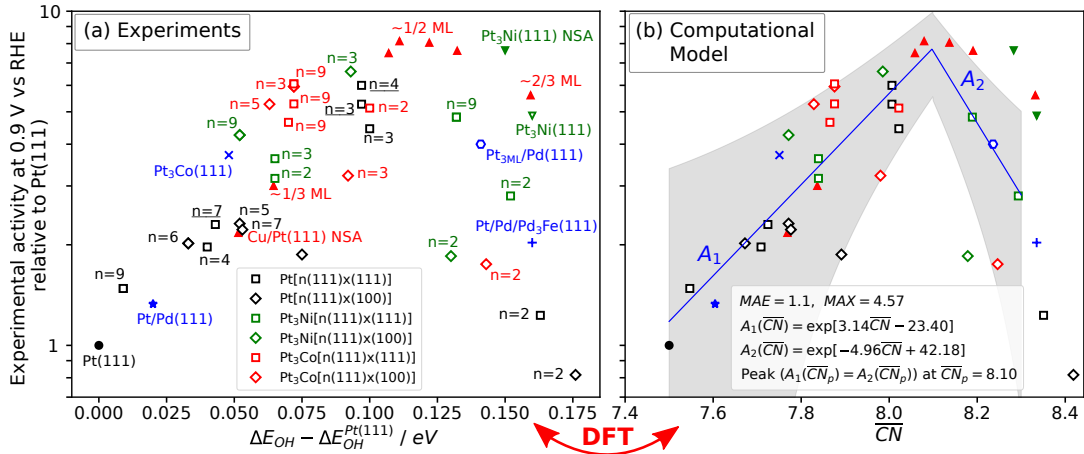
Figure 2.4: (a) Relative experimental activities of various Pt stepped surfaces (forming terrace widths of length n) and Pt alloy fcc(111) single-crystals are plotted vs experimental *OH binding energies: (black open squares) Pt stepped surfaces; (green open squares) Pt$_3$Ni stepped surfaces; (red open squares) Pt$_3$Co stepped surfaces; (red up-pointing traingle) Cu/Pt(111) NSAs with full and partial (1/3 ML, 1/2 ML, 2/3 ML) surface Cu content; (full green down-pointing triangle) Pt$_3$Ni(111) NSA; (open green down-pointing triangle) bulk Pt$_3$Ni(111); (blue star) one monolayer of Pt on Pd(111); (blue plus) monolayer of Pt on annealed Pd$_3$Fe(111) electrode with one segregated Pd layer; (open blue octahedron) three monolayers of Pt on Pd(111); (blue x) bulk Pt$_3$Co(111). Pt stepped surfaces, which are highlighted by underlined terrace widths of length $n = 3$, $n = 4$, $n = 7$, are taken from Ref. 50. Remaining data is taken from Ref. 41 and sources therein. The catalytic activities are measured at 0.9 V vs RHE in 0.1 M HCLO$_4$. (b) The linear scaling relation in Figure 2.3 maps the experimental binding energy in (a) onto $\overline{CN}$. Linear regression data of the increasing and decreasing activity functions A_1 and A_2, respectively, are provided in the inset. The gray area covering $\pm$2MAE around the linear fit contains 92% of the calculated data points. Adapted with permission from Ref. 103. Copyright 2018 American Chemical Society.

is captured by fit functions A_1 and A_2, which feature a peak in activity at $\overline{CN}_{peak}$. The activity follows an exponential trend with respect to $\overline{CN}$. Hence, the fit functions are increasing and decreasing exponential functions yielding

$$
\begin{aligned}
A_1(\overline{CN}) &= \exp(3.14\,\overline{CN} - 23.40)\ , \\
A_2(\overline{CN}) &= \exp(-4.96\,\overline{CN} + 42.18)\ ,
\end{aligned}
\tag{2.13}
$$

as provided in the inset of Figure 2.4b. The activity trend agrees well with the above-discussed Sabatier analysis,[43] where enhanced activities over Pt(111) are determined for sites with $7.5 < \overline{CN} \leq 8.3$. The activity peak at $\overline{CN}_{peak} = 8.1$ corresponds to $\Delta E_{OH} - \Delta E_{OH}^{Pt(111)} \approx 0.115 eV$, which boosts the Pt(111) activity by a factor of $A_{volc}(8.1) \approx 7.65$.

Beyond the peak at larger $\overline{CN}$ in Figure 2.4, the activity trend is widely dispersed. At small $\overline{CN}$, sites may be affected by oxygenated species, which block the catalysis at these centers.[105] Thus, activity contributions from sites with $\overline{CN} < 7.5$ and $\overline{CN} > 8.3$ are neglected in the computational model.

For activity prediction relative to Pt(111), the activity contributions for all nanoparticle atoms are summed up. Therefore, nanoparticle activities are obtained by

$$
j_{relNP} = \sum_i^{N_{NP}} \Theta\big(\overline{CN}(i) - 7.5\big) \Theta\big(8.3 - \overline{CN}(i)\big)\ A_{volc}\big(\overline{CN}(i)\big)
\tag{2.14}
$$

relative to the activity of one site on Pt(111). N_{NP} denotes the total number of atoms in the nanoparticle and the Heaviside step function $\Theta(x)$ yields zero activities for $\overline{CN}(i) < 7.5$ or $\overline{CN}(i) > 8.3$ as discussed above. In the remainder of this section, we extend the model to activity and mass activity prediction in absolute units.

Experimentally, Pt(111) yields $j_{Pt(111)} = 2\ mA/cm^2$ specific activity.[43] The density of Pt atoms on the Pt(111) surface is given by $d_{Pt(111)} = 1.503 \times 10^{15}\ cm^{-2}$. Thus, based on j_{relNP} above, absolute catalytic activities are calculated by

$$
j_{NP} = \frac{j_{Pt(111)}}{d_{Pt(111)}} j_{relNP} \approx 1.331 \times 10^{-18}\ A\ j_{relNP}\ .
\tag{2.15}
$$

Using the mass of one Pt atom given by $m_{Pt} = 195.084\ u$, catalytic mass activities are predicted by

$$
j_{mNP} = \frac{j_{NP}}{m_{Pt} N_{NP}} \approx \frac{4.107\ A/mg_{Pt}}{N_{NP}} j_{relNP}
\tag{2.16}
$$

in absolute units of A/mg_{Pt}.

To assess the accuracy of the computational model, we compare predicted mass activities with experimental measurements from *Perez-Alonso et al.*[57] for nanoparticles of various sizes (see Figure 2.5). The experimental nanoparticles have sphere-like shapes,[57] which are modeled by spherical nanoparticles (see Figure 2.2). Experimental size distributions are considered in computational predictions by averaging over the mass activities of nanoparticles within the experimental size ranges.

The computational mass activity predictions, which are given in absolute units of A/mg$_{Pt}$, are within the error intervals of the experimental measurements; except for the smallest diameter at 2 nm where corrosion effects may have degraded the nanoparticle structure in the experiment.[57] Thus, the computational model provides mass activity predictions in precise agreement with experiments.
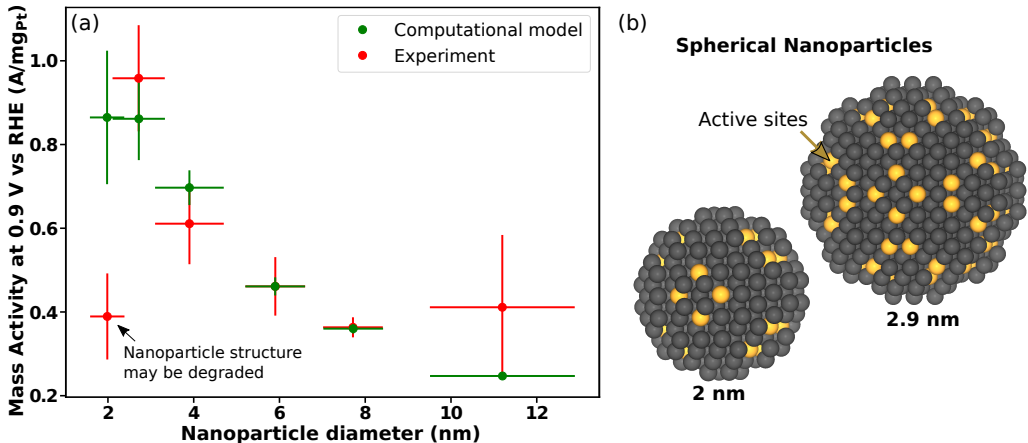
Figure 2.5: (a) Computational predictions of mass activities (green dots) compared to experimental mass activities from *Perez-Alonso et al.*[57] (red dots) for nanoparticles of various sizes. Vertical error bars for computational mass activities represent the standard error of the mean. Size distributions employed in the computational model correspond to those in the experimental study. (b) Nanoparticles with 2 nm and 2.9 nm size as employed for the computational predictions. Active sites are highlighted in yellow. Adapted with permission from Ref. 103. Copyright 2018 American Chemical Society.

The computational model can be extended to mass activity predictions on strained Pt sites, which we introduce in Ref. 102. For unstrained sites, eq 2.7 states that $\overline{CN} = \overline{CN}^*$. Because *OH adsorption energies on strained Pt sites approximately follow the same linear trend in $\overline{CN}^*$ as on unstrained Pt sites,[70] $\overline{CN}^*$ can be used (instead of $\overline{CN}$) in the activity-volcano in Figure 2.4b to capture strain effects.

2.4   Tailoring Nanocatalyst Shapes by the Superformula and Particle Swarm Optimization

This concept is published and reproduced in part with permission from Ref. 98, Nanoscale Adv., 2019, 1 (8), 2901-2909. Published by The Royal Society of Chemistry (RSC).

On the experimental side, synthesis and characterization of several thousand nanocatalysts is expensive and costly in time. Thus, effective computational screenings of nanostructures can provide prospective electrocatalysts for synthesis. Nonetheless, computational mass activity prediction within feasible computation times is demanding. The concept of $\overline{CN}$ provides seminal knowledge of active local site structures, but it does not disclose how high ratios of active sites can be incorporated in stable nanostructures with high mass activities.

Herein, we propose a theoretical framework to screen and optimize Pt nanocatalysts toward highest mass activity at controllable size distribution and decent mechanical stability (see Figure 2.6). *Gielis'* Superformula[106] comprises a continuous parameter space to generate various kinds of shapes. We introduce a generalization of the Superformula in three dimensions[107, 108] to create a wide variety of continuous and symmetric shapes, because symmetries are expected to facilitate synthesis of tailored nanocatalysts.[109] The shapes are filled with Pt atoms, but low-coordinated sites with $cn < 6$ are avoided to account for decent stability under ORR conditions. This constraint is rationalized by the observation, that Pt mesostructures with minimal coordination around $cn = 6$ have improved stability over ETEK commercial Pt/C catalysts in experiments.[55] Resulting nanostructures are evaluated in terms of mass activity using the above-discussed computational model. The nanostructures are carefully optimized toward highest mass activity by Penalty Attractive and Repulsive Particle Swarm Optimization (PARPSO)[110] in several hundred iterative steps.
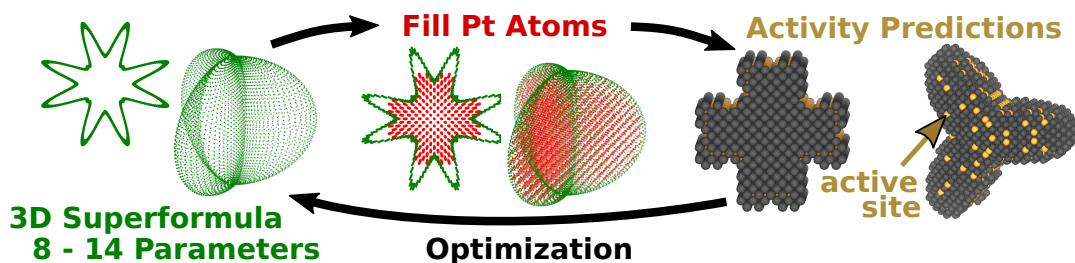
Figure 2.6: Optimizing nanocatalyst shapes toward highest activity. Superformula generated nanoshapes are filled with Pt atoms, but low-coordinated sites with $cn < 6$ are avoided. Resulting nanostructures are evaluated upon activity using the computational model. The nanostructures are optimized toward highest activity by Particle Swarm Optimization.

Superformula in three dimensions

A three-dimensional version of the Superformula has been used to for nanophotonic[108] and dielectric[107] materials. We generalize this Superformula in three dimensions, so that the Superformula shapes fulfill C3 or C4 rotational symmetries with respect to the z-axis. Around the x- and y-axes, all Superformula shapes are C2 symmetric. We propose two distinct Superformula types, which are derived from spherical coordinates and cylindrical coordinates, respectively. Nanostructures, which are created from the Superformula of cylindrical type, can feature active local site structures at concave kinks yielding superior mass activities.

The generalized Superformula in three dimensions derived from spherical coordinates is given by

$$
\begin{aligned}
x &= \eta \; r_1(\Phi_r(\Phi) + \Phi_0) \cos(\Phi) \; r_2(\Theta) \cos(\Theta) \\
y &= \eta \; r_1(\Phi_r(\Phi) + \Phi_0) \sin(\Phi) \; r_2(\Theta) \cos(\Theta) \\
z &= \eta \; r_2(\Theta) \sin(\Theta) \; ,
\end{aligned}
\tag{2.17}
$$

where

$$
\begin{aligned}
r_1(\Phi) &= \left[\left| \frac{\cos(\frac{m^{(\Phi)}}{4}\Phi)}{a^{(\Phi)}} \right|^{n_2^{(\Phi)}} + \left| \frac{\sin(\frac{m^{(\Phi)}}{4}\Phi)}{b^{(\Phi)}} \right|^{n_3^{(\Phi)}} \right]^{-1/n_1^{(\Phi)}} \\
r_2(\Theta) &= \left[\left| \frac{\cos(\frac{m^{(\Theta)}}{4}\Theta)}{a^{(\Theta)}} \right|^{n_2^{(\Theta)}} + \left| \frac{\sin(\frac{m^{(\Theta)}}{4}\Theta)}{b^{(\Theta)}} \right|^{n_3^{(\Theta)}} \right]^{-1/n_1^{(\Theta)}} .
\end{aligned}
\tag{2.18}
$$

14 parameters span the Superformula in eq 2.17. Six of them, that are $m^{(\Phi)}$, $n_1^{(\Phi)}$, $n_2^{(\Phi)}$, $n_3^{(\Phi)}$, $a^{(\Phi)}$, $b^{(\Phi)}$ are associated with the azimuthal angle Φ. Further six paramters, namely $m^{(\Theta)}$, $n_1^{(\Theta)}$, $n_2^{(\Theta)}$, $n_3^{(\Theta)}$, $a^{(\Theta)}$, $b^{(\Theta)}$, are related to the altitude angle Θ. The 13th parameter η determines the size of the shape. The three dimensional space is spanned by the angular variables $\Phi \in [-\pi, \pi]$ and $\Theta \in [-\pi/2, \pi/2]$. The 14th parameter Φ_0 controls the selected section of the Φ domain, which is discussed below.

The functions

$$
\Phi_r(\Phi) = \begin{cases} |\Phi| - 2\pi/3 & \text{, if } |\Phi| \geq 2\pi/3 \\ 2\pi/3 - |\Phi| & \text{, if } |\Phi| < 2\pi/3 \; \wedge \; |\Phi| \geq \pi/3 \\ |\Phi| & \text{, if } |\Phi| < \pi/3 \end{cases}
\tag{2.19}
$$

for C3 symmetry and

$$
\Phi_r(\Phi) = \begin{cases} \pi - |\Phi| & \text{, if } |\Phi| \geq 3\pi/4 \\ |\Phi| - \pi/2 & \text{, if } |\Phi| < 3\pi/4 \; \wedge \; |\Phi| \geq \pi/2 \\ \pi/2 - |\Phi| & \text{, if } |\Phi| < \pi/2 \; \wedge \; |\Phi| \geq 1\pi/4 \\ |\Phi| & \text{, if } |\Phi| < \pi/4 \end{cases}
\tag{2.20}
$$

for C4 symmetry map the full domain of the variable $\Phi \in [-\pi, \pi]$ onto the subset $\Phi_r(\Phi) \in [0, c]$, so that $c = \pi/3$ for C3 symmetry and $c = \pi/4$ for C4 symmetry. The choice of the parameter Φ_0 in range of $[0, \pi]$, which is included in eq 2.17, allows to select any section of the full domain $\Phi \in [-\pi, \pi]$ of the Superformula shape. The choice of the identity function $\Phi_r(\Phi) = \Phi$ and $\Phi_0 = 0$ reduces the generalized Superformula in eq 2.17 to the less symmetric Superformula in three dimensions, which is applied in Refs.[107, 108]

Moreover, the Superformula derived from cylindrical coordinates is given by

$$
\begin{aligned}
x &= \eta\, r_1(\Phi) \cos(\Phi) \\
y &= \eta\, r_1(\Phi) \sin(\Phi) \\
z &= z
\end{aligned}
\tag{2.21}
$$

The cylindrical Superformula is spanned by 8 parameters in total.

Particle swarm optimization

Nanostructures are optimized toward highest mass activity by Penalty Attractive and Repulsive Particle Swarm Optimization (PARPSO).[110] The optimization algorithm includes four overall steps, which are illustrated in Figure 2.6:

1. $N = 50$ Superformula shapes are initialized randomly. Each shape j is associated with a set $\boldsymbol{x}_j^k$ of 14 or 8 parameters depending on the type of Superformula. k denote the iterative step.

2. Each Superformula shape is filled with Pt atoms, but low-coordinated sites with $cn < 6$ are avoided.

3. Mass activities of all $N = 50$ nanostructures are predicted by the computational model.

4. The Superformula parameters of all $N = 50$ nanoparticle ensembles are optimized toward highest mass activity by PARPSO. Besides random fluctuations, PARPSO considers information about previously evaluated mass activities to update parameter sets toward highest mass activity. Subsequently, the algorithm continues with step 2, unless the maximum iteration steps k_{max} are reached.

Optimizations are performed iteratively with $k_{max} = 604$ to $k_{max} = 800$ maximum steps. This takes only few days of computation time using multiprocessing in Python.

Three tradeoffs are considered during nanostructure optimization in step 4:

- Each parameter set $\boldsymbol{x}_j^k$ is optimized with respect to the best parameters $\boldsymbol{p}_{best,j}^k$ in the history of the parameter set j and the overall best parameters $\boldsymbol{g}_{best}^k$ observed in the history out of all parameter sets.

- The variable d^k, which takes either 1 or -1, trades off the search near $\boldsymbol{p}_{best,j}^k$ against $\boldsymbol{g}_{best}^k$. Upon d^k, the search may be driven toward inverse direction.

- The penalty factor w_2 repulses each parameter set from the worst parameters $\boldsymbol{g}_{worst}^k$ observed in the history out of all parameter set.

In each iterative step k, parameter sets are updated as $\boldsymbol{x}_j^{k+1} = \boldsymbol{x}_j^k + \boldsymbol{V}_j^{k+1}$ with

$$
\begin{aligned}
\boldsymbol{V}_j^{k+1} =& w_1^k \boldsymbol{V}_j^k + d^{k+1} \big[c_1 r_1^k (\boldsymbol{p}_{best,j}^k - \boldsymbol{x}_j^k) + c_2 r_2^k (\boldsymbol{g}_{best}^k - \boldsymbol{x}_j^k) \big] \\
& - w_2^k c_3 r_3^k (\boldsymbol{g}_{worst}^k - \boldsymbol{x}_j^k) \ .
\end{aligned}
\tag{2.22}
$$

The variable d^{k+1} is given by

$$
d^{k+1} = \begin{cases} -1 \ , \text{ if } \ d^k > 0 \text{ and } d_{diversity}^k < d_{low} \\ 1 \ , \text{ if } \ d^k < 0 \text{ and } d_{diversity}^k > d_{high} \\ d^k, \text{ otherwise } \ . \end{cases}
\tag{2.23}
$$

The diversity function

$$
d_{diversity}^k = 1/N \sum_{j=1}^{N} d_{div,j}^k
\tag{2.24}
$$

with

$$
d_{div,j}^k = \begin{cases} 0 \ , \text{ if } \ |\boldsymbol{p}_{best,j}^k - \boldsymbol{x}_j^k| < |\boldsymbol{g}_{best}^k - \boldsymbol{x}_j^k| \\ 1 \ , \text{ otherwise} \end{cases}
\tag{2.25}
$$

trades off the search near $\boldsymbol{p}_{best,j}^k$ against $\boldsymbol{g}_{best}^k$. Thus, if most parameter sets are close to $\boldsymbol{p}_{best,j}^k$ ($\boldsymbol{g}_{best}^k$), the diversity $d_{diversity}^k$ will take values near zero (one), which may drive the search toward inverse direction in eq 2.22. To this end, the thresholds $d_{low} = 0.4$ and $d_{high} = 0.6$ yield appropriate tradeoffs.

The penalty factor w_2^k is given by

$$
w_2^k = \frac{min\Big(\big[|\boldsymbol{g}_{worst}^k - \boldsymbol{x}_1^k|, |\boldsymbol{g}_{worst}^k - \boldsymbol{x}_2^k|, ..., |\boldsymbol{g}_{worst}^k - \boldsymbol{x}_N^k| \big] \Big)}{|\boldsymbol{g}_{worst}^k - \boldsymbol{x}_j^k|} \ ,
\tag{2.26}
$$

which pushes parameter sets away from the worst observed parameters. The prefactor

$$w_1^k = w_{1,max} - (w_{1max} - w_{1min})\frac{k-1}{k_{max}-1} \qquad (2.27)$$

decelerates the search velocities upon increasing iterative steps from $k = 1$ to $k = k_{max}$, where $w_{1max} = 0.9$ and $w_{1min} = 0.1$. Three uniformly distributed random numbers r_1, r_2, and r_3 are considered in each iterative step in range of $[0,1[$. The three overall constants are chosen as $c_1 = 2$, $c_2 = 2$, and $c_3 = 0.4$.

Thus, computational screenings are strongly aligned to most active nanocatalysts with respect to mass, but nanostructures with somewhat lower than optimum mass activity are also taken into account.

2.5   Machine Learning Prediction of Strain

This concept is published and reproduced in part with permission from Ref. 102, J. Phys. Chem. Lett., 2020, 11 (5), 1773-1780. Copyright 2020 American Chemical Society.

In core-shell nanoparticles, cheaper and more abundant metals than Pt can be used in the core, but the catalysis is driven on active Pt shells (see Figure 2.7). The lattice mismatch between core metal and Pt shell induces strain, which changes adsorption energies of reaction intermediates on the nanoparticle surface. Therefore, optimal strain degrees can shift adsorption energies toward enhanced activities, which is predominantly controlled by nanoparticle size, core material, and shell thickness. Thus, strain engineering on core-shell nanoparticles enables a promising vast design space for the ORR, though effective computational screenings are demanding.[77,78,86,87]

Herein, to facilitate screening the vast core-shell design space, we propose a machine
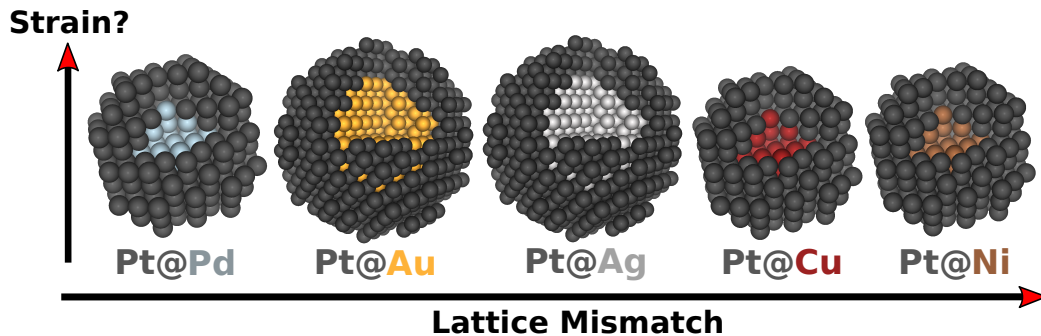
Figure 2.7: Relative lattice mismatches in core-shell nanoparticles between Pt shell and fcc core metals. Strains for various nanoparticle sizes are predicted by the herein proposed machine learning approach.

learning approach for strain prediction on core-shell nanoparticles with site-specific precision. More specifically, the machine learning models predict the strained coordination cn^* (see eq 2.1), from which site-specific strain in eq 2.3 can be calculated. We examine fcc core metals Ni, Cu, Pd, Au, and Ag on Pt shell thicknesses of 2-3 and 3-4 monolayers, for which ligand effects are shown to be negligible and activity enhancements are mainly attributed to strain effects.[39,84,85,89–92] Machine learning models are trained and tested on nanoparticles, which are structure optimized toward the minimum energy by effective medium theory (EMT).[111] Based on machine learning predicted cn^*, we determine $\overline{CN}^*$ and extend the above-discussed computational model to activity forecasts of strained Pt nanocatalysts. Thus, for activity screenings of core-shell nanoparticles, broad ranges of sizes can be evaluated by machine learning, where only few nanoparticles are structure optimized for training.

Kernel Ridge Regression

We use Kernel Ridge Regression (KRR) with Radial Basis Function (RBF) kernel from the Scikit-learn[112] module in Python. KRR corresponds to a least square fit with an increasing penalty toward larger fitting coefficients $\boldsymbol{w} = (w_1, w_2, ..., w_N)^T$.[113,114] The KRR minimizes the penalized sum of squares

$$\underset{\boldsymbol{w} \in \mathbb{R}^M}{\mathrm{argmin}}\left[||\boldsymbol{Xw} - \boldsymbol{y}||_2^2 + \alpha||\boldsymbol{w}||_2^2\right] . \tag{2.28}$$

We define $\boldsymbol{X} = (x_{i,j})$ as the $(N \times M)$-dimensional matrix of the inputs, which includes M features for N data points, and $\boldsymbol{y} = (y_1, y_2, ..., y_N)^T$ are the outputs.

The solution of $\boldsymbol{w}$, which minimizes the argument in eq 2.28, is found to be

$$\boldsymbol{w} = (\boldsymbol{X}^T\boldsymbol{X} + \alpha\boldsymbol{I}_M)^{-1}\boldsymbol{X}^T\boldsymbol{y} = \boldsymbol{X}^T(\boldsymbol{X}\boldsymbol{X}^T + \alpha\boldsymbol{I}_N)^{-1}\boldsymbol{y} , \tag{2.29}$$

where $\boldsymbol{I}_N$ is the identity matrix of N-dimensions. The identity from linear algebra

$$(P^{-1} + B^T R^{-1} B)^{-1} B^T R^{-1} = P B^T (BPB^T + R)^{-1} , \tag{2.30}$$

is used in the second step. The function $\Phi : \mathbb{R}^M \mapsto H$ maps the features onto the Kernel space, which is a Hilbert space, with a Kernel function $K : \mathbb{R}^M \times \mathbb{R}^M \mapsto \mathbb{R}$. In Kernel space $\boldsymbol{X} \mapsto \Phi(\boldsymbol{X})$, eq 2.29 reads

$$\begin{aligned}
\boldsymbol{w} &= \Phi(\boldsymbol{X})^T\big(\Phi(\boldsymbol{X})\Phi(\boldsymbol{X})^T + \alpha\boldsymbol{I}_N\big)^{-1}\boldsymbol{y} \\
&= \Phi(\boldsymbol{X})^T\big(\boldsymbol{K} + \alpha\boldsymbol{I}_N\big)^{-1}\boldsymbol{y} \\
&= \Phi(\boldsymbol{X})^T\boldsymbol{\beta} \\
&= \sum_i \boldsymbol{\beta}_i\,\Phi(\boldsymbol{X_i}) ,
\end{aligned} \tag{2.31}$$

where the index i denotes the i-th row. $\boldsymbol{K} = \Phi(\boldsymbol{X})\Phi(\boldsymbol{X})^T$ is the Gram matrix (also called Kernel matrix). This Gram matrix is positive definite and therefore invertible. To predict the output $\boldsymbol{y}'$ of a new data point with features $\boldsymbol{x}' = (x'_1, ..., x'_M)$, $\Phi(\boldsymbol{x}')$ is projected onto the solution as

$$\boldsymbol{y}' = \boldsymbol{w}\ \Phi(\boldsymbol{x}') = \sum_i \boldsymbol{\beta}_i\ \Phi(\boldsymbol{X}_i)\ \Phi(\boldsymbol{x}')\ , \tag{2.32}$$

where $K(\boldsymbol{X}_i, \boldsymbol{x}') = \Phi(\boldsymbol{X}_i)\Phi(\boldsymbol{x}')$ is the kernel function. Therefore, instead of explicitly mapping into feature space using Φ, the kernel function can be employed. This is known as dual representation.[113] Thus, the computation time is independent of the number of features M. The RBF kernel function (also called Gaussian kernel) from the Scikit-learn[112] module reads

$$K(\boldsymbol{X}_i, \boldsymbol{x}') = \exp\left(-\gamma\ ||\boldsymbol{X}_i - \boldsymbol{x}'||_2^2\right)\ . \tag{2.33}$$

In this work, we use the penalty prefactor $\alpha = 10^{-5}$ and the default value of $\gamma = 1/M$ for all machine learning predictions. We have $M = 22$ features.

Machine Learning Features

Feature	Abbreviation
coordination number	$cn(i)$
generalized coordination number	$\overline{CN}(i)$
partial distribution function	$PDF(i, r)$
distance to alloy atoms	$d_{alloy}(i)$
interatomic distance from Vegard's law	$d_{veg}(i)$

Table 2.1: Geometrical machine learning features evaluated for atom i and radius r.

To predict strained coordinations cn^* on core-shell nanoparticle atoms, we combine KRR machine learning with the geometric features in Table 2.1. The features are fast and cheap to calculate. Features are determined with site-specific precision for each nanoparticle atom i. All features are evaluated on non-structure optimized core-shell nanoparticles, where the atomic positions are equivalent to the positions in non-structure optimized pure Pt nanoparticles as shown in Figure 2.2. The features create a link between the nanoparticle shape and bimetallic configuration:

- $cn(i)$ in eq 2.6 and $\overline{CN}(i)$ in eq 2.7 describe the local-site structure, but without consideration of the bimetallic configuration.

- The partial distribution function for one atom i

$$PDF(i,r) = \left[\frac{1}{a_{nn}^{Pt} \sum_{j \neq i}^{N_{tot}} \Theta(r - |\boldsymbol{r}_i - \boldsymbol{r}_j|)} \sum_{j \neq i}^{N_{tot}} \Theta\big(r - |\boldsymbol{r}_i - \boldsymbol{r}_j|\big) \, a_{nn}(j) \right] - 1$$

(2.34)

sums up the bulk interatomic distance $a_{nn}(j)$ (normalized by the Pt bulk interatomic distance a_{nn}^{Pt}) for all atoms j, which are enclosed within radius r around the atom i. Bulk interatomic distances are provided in eq 2.2. N_{tot} denotes the total number of nanoparticle atoms. Thus, the PDF captures the deviation between the bimetallic core-shell configuration and the atomic configuration in pure Pt nanoparticles. Variations of the PDF have been previously applied to examine nanostructures[115] with KRR machine learning.[116–119]

We use $PDF(i,r)$ for 18 different radii between 0.33-5.05 nm, which are given by

$$r(n) = n \, a_{nn}^{Pt} + (a_{sn}^{Pt} - a_{nn}^{Pt})/2$$

(2.35)

for integer $n = 1, 2, \ldots, 18$ and Pt bulk second nearest neighbor distance $a_{sn}^{pt} \approx 0.392 \, nm$. The sum over $a_{nn}(j)$ in eq 2.34 is illustrated in Figure 2.8.
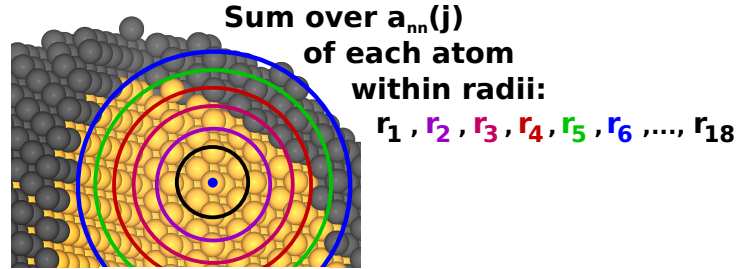
Figure 2.8: The $PDF(i,r)$ sums up bulk interatomic distances $a_{nn}(j)$ for any atom j, which is located within radius $r = r_1, .., r_{18}$ around atom i.

- $d_{alloy}(i)$ is defined as mean distance from atom i to all neighbored alloy atoms up to the second nearest alloy atom.

- $d_{veg}(i)$ provides an estimate for the interatomic distance based on Vegard's law. For atom i, we iteratively compute

$$d_{veg}^{s+1}(i) = \frac{d_{veg}^s(i) + \sum_j^{n_i} d_{veg}^s(j)}{1 + n_i}$$

in iterative steps s with initial condition $d_{veg}^{s=0}(i) = a_{nn}(i)$. Atom j is nearest

neighbor of i, which are n_i nearest neighbors in total. If the criterion

$$\left|\frac{d_{veg}^{s+1}(i) - d_{veg}^s(i)}{d_{veg}^{s+1}}\right| \leq 0.001$$

for small changes is reached, the iteration will be terminated.

Effective Medium Theory

Effective medium theory (EMT)[111] describes the total energy for systems of the six fcc metals Ag, Au, Pt, Pd, Cu, Ni and their alloys. In EMT, the total energy is described by the energy of the perfect fcc crystal plus the energy difference between the perfect fcc crystal and the real crystal structure. The total energy is then calculated using potentials fitted to 7 parameters per fcc metal, which are determined by self-consistent calculations and experiments. We use the EMT implementation in the ASAP calculator from the Atomic Simulation Environment (ASE).[120]

Machine Learning Accuracy

We exemplify machine learning accuracies of cn^* predictions on core-shell nanoparticles with 2-3 monolayer Pt shell thickness. The machine learning model is trained on nanoparticle sizes between 1.6-5.4 nm in 0.2 nm size intervals (see Figure 2.9), which are structure optimized toward the minimal energy structure by EMT and the quasi-Newton method. Interjacent sizes from 1.7-5.3 nm are employed for testing.
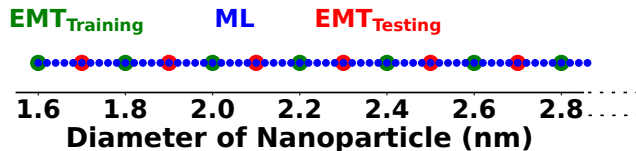
Figure 2.9: Nanoparticle sizes employed for training (green), for testing (red), and for machine learning predictions of strain. The size scale is truncated at 2.86 nm. Reprinted with permission from Ref. 102. Copyright 2020 American Chemical Society.

We first train and test the machine learning model for each core metal separately. Training sets comprise each 2nd atom of the nanoparticles from training sets. For testing, we employ each atom of the nanoparticles from testing sets. Figure 2.10 shows that the mean relative error (MRE) decreases toward smaller lattice mismatch between Pt shell and core metal. Lattice mismatches decrease in the order Ni > Cu > Ag > Au > Pd (see Figure 2.7), so that the MREs decrease as 1.54% (Ni), 0.63 % (Cu), 0.15% (Ag, Au), and 0.07% (Pd).

For cross predictions, we train the machine learning model on each 5th atom of nanoparticles of 4 core metals. We then predict cn^* on atoms of nanoparticles with the remaining core metal. For instance, for cn^* cross prediction on PtAg, the
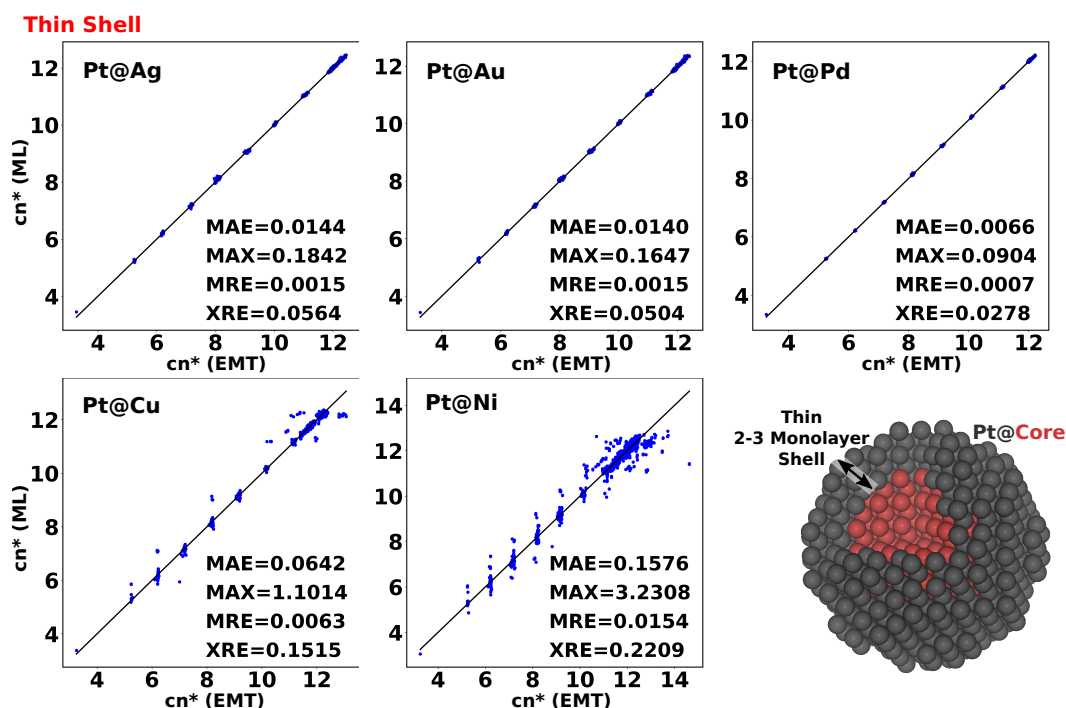
Figure 2.10: Machine learning accuracies of cn^* prediction trained for each core metal separately. cn^* predicted from machine learning (ML) is shown versus cn^* calculated by effective medium theory (EMT). Mean absolute error (MAE), maximum absolute error (MAX), mean relative error (MRE), and maximum relative error (XRE) determined on the testing set are provided in the insets. Size scale is truncated at 2.86 nm. Adapted with permission from Ref. 102. Copyright 2020 American Chemical Society.

machine learning model is trained on PtAu, PtPd, PtCu, and PtNi. Therefore, our cross predictions can be considered as cross validation. It is demonstrated in Figure 2.11 that the cross predictions have similar accuracies as the predictions within same core metals presented in Figure 2.10. Thus, the cross predictions confirm that our trained machine learning models are not overfitted.
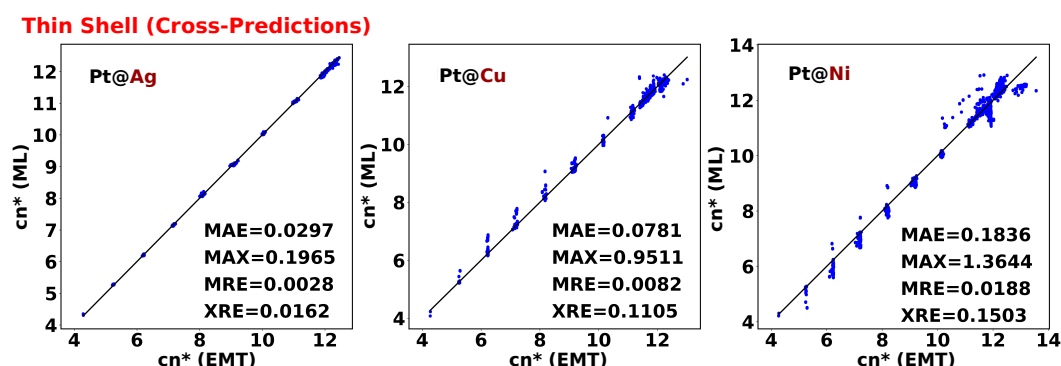
Figure 2.11: Cross prediction accuracies between cn^* predicted by machine learning (ML) predicted and calculated byeffective medium theory (EMT). Adapted with permission from Ref. 102. Copyright 2020 American Chemical Society.

3   Publications

3.1   Oxygen Reduction Reaction: Rapid Prediction of Mass Activity of Unstrained Nanostructured Platinum Electrocatalysts

In this study, we build a computational model to predict mass activities on pure Pt electrocatalysts for the ORR in absolute units of A mg_{Pt}^{-1}. Experimental data from literature demonstrate a volcano-shaped activity trend between $^*OH$ adsorption energies and ORR activities. Theoretical DFT studies show that $^*OH$ adsorption energies are linearly related with the generalized coordination number $\overline{CN}$. We capitalize on both relations to link the experimental ORR activities with $\overline{CN}$. Therefore, mass activities for the ORR can be predicted upon nanoparticle geometries described by $\overline{CN}$. This realizes feasible computation times in comparison to theoretical predictions solely based on DFT. Furthermore, the rapid activity predictions allow for the consideration of nanoparticle size distributions, which requires activity predictions for all nanoparticles within the respective size ranges.

The prediction accuracy of the computational model was tested on two experimental datasets involving nanoparticles of various sizes. Mass activity predictions reproduce the experimental activity trends. With respect to absolute units, the two
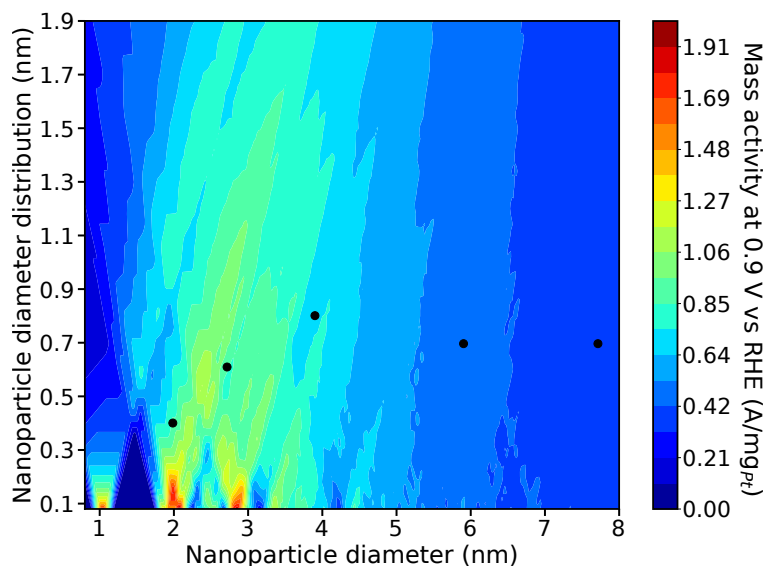
Figure 3.1: Predicted mass activities for the ORR on spherical nanoparticles, which depend on the nanoparticle diameter and the nanoparticle diameter distribution. Experimental data (black dots) from Ref. 57 are included. Reprinted with permission from Ref. 103. Copyright 2018 American Chemical Society.

experiments differ significantly by 1 order of magnitude. However, precise quantitative agreement in absolute units has been established between the predictions from the computational model and one experimental dataset from *Perez-Alonso et al.*[57]

Beyond thitherto available experiments, this study provides predictions of highly active nanoparticles (see Figure 3.1). The promising nanoparticles with highest activities are predicted at nanoparticle sizes near 1, 2, 3 nm toward small size distributions around 0.1 nm and below. Furthermore, it is important to note that mass activities become increasingly sensitive to small changes in the nanoparticle structure toward small nanoparticle sizes. In contrast, toward larger sizes, the structure sensitivity decreases and therefore, broadening the size distributions keeps the mass activities on similar levels.

Individual contributions:

I substantially contributed to the ideas and implementations of the computational model and its application in this study. I identified and considered the high importance of nanoparticle size distributions to predict mass activities in close agreement with experiments. I translated the computational predictions into synthesis guidelines by designing and implementing the computational model approriately. I authored the manuscript considering the broad expertise on catalysis modeling, synthesis, and characterization provided by the co-authors.

3.2 Optimizing the Size of Platinum Nanoparticles for Enhanced Oxygen Electro-Reduction Mass Activity

In this work, we doubled the commercial activity of ORR catalysts by leveraging computational design in catalyst synthesis. We employ the computational model (presented in the previous publication above) to identify nanoparticle sizes with optimal mass activities. By computational screening, highest mass activities of 2.3 A mg_{Pt}^{-1} are predicted for single nanoparticles at 1.1, 2.07, and 2.87 nm sizes (see Figure 3.2). To compare the mass activities with experimental results, we take size distributions
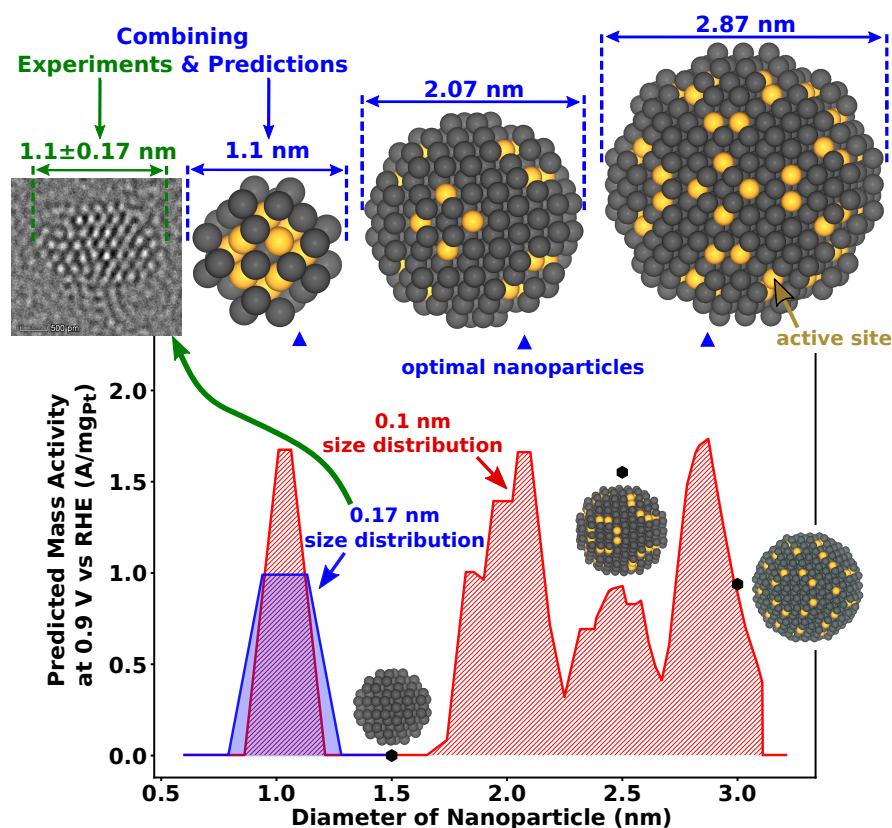
Figure 3.2: Mass activities predicted by the computational model. Optimal nanoparticles (blue triangles) are identified at diameters of 1.1 nm, 2.07 nm, and 2.87 nm. Three less active nanoparticles (green hexagons) are exemplified at 1.5 nm, 2.5 nm, and 3 nm. The red and blue curves show predicted mass activities for nanoparticles with 0.1 nm and 0.17 nm size distribution, respectively. Adapted with permission from Ref. 101. Copyright 2019 Wiley.

into account. For the optimal nanoparticles, small size distributions of 0.1 nm reduce their superior mass activities to around 1.25 A mg_{Pt}^{-1} at 1.1 nm and 1.7 A mg_{Pt}^{-1} at 2.07 and 2.87 nm. Moreover, the slightly larger size distribution of 0.17 nm, which has been experimentally realized in this study, yields 0.99 A mg_{Pt}^{-1} for the 1.1 nm sized nanoparticles.

Following the computational predictions, we accomplished synthesis of 1.1±0.17 nm sized Pt nanoparticles using a metal-organic framework. The synthesized nanoparticles have measured mass activities of 0.87±0.14 A mg_{Pt}^{-1}, which coincide with the computational predictions (0.99 A mg_{Pt}^{-1}) with respect to the error intervals. Activity measurements of 1500 cycles are performed to examine stabilities. Similar stabilities have been observed for the 1.1 nm sized nanoparticles compared to Tanaka commercial Pt/C electrocatalysts.

To sum up, we synthesized 1.1 nm nanoparticle catalysts by computational design, which have twice the mass activity and comparable stability of commercial Pt/C catalysts (0.42 A mg_{Pt}^{-1}).

Individual contributions:

The broad scientific scope of this work has been realized by interdisciplinary collaboration between Alessio Gagliardi and I (catalyst modeling), Kathrin Kratzl and Roland A. Fischer (catalyst synthesis), Batyr Garlyyev and Aliaksandr Bandarenka (catalyst characterization), and further crucial experimental contributions by the co-authors. I substantially contributed to the ideas and implementations of the computational predictions with regard to their deployment in nanoparticle synthesis. I identified the nanoparticles with optimal activity by computational screenings, provided the associated catalyst designs, and presented the computational results graphically. I authored the computational part of the manuscript as well as parts of the abstract, introduction, and conclusion.

3.3   Fast Identification of Optimal Pure Platinum Nanoparticle Shapes and Sizes for Efficient Oxygen Electroreduction

Herein, we propose tailored electrocatalysts with superior mass activities beyond spherical nanoparticle shapes. Electrocatalyst shapes are constructed by the Superformula,[106] which provides a parametrization for a wide variety of different nanoshapes. More specifically, we propose a generalization of the Superformula in three spatial dimensions to create nanoshapes with C3 or C4 symmetries, because symmetries are expected to facilitate synthesis of tailored nanocatalysts. The nanostructured electrocatalysts are built by filling the nanoshapes with Pt atoms from the fcc bulk geometry, but low-coordinated sites with $cn < 6$ are avoided to account for high stability under ORR conditions. We employ the computational model (presented in the previous publication above) to predict mass activities upon the nanostructure. The electrocatalyst shapes and sizes are optimized toward highest activity by Penalty Attractive and Repulsive Particle Swarm Optimization (PARPSO)[110] in several hundred itera-
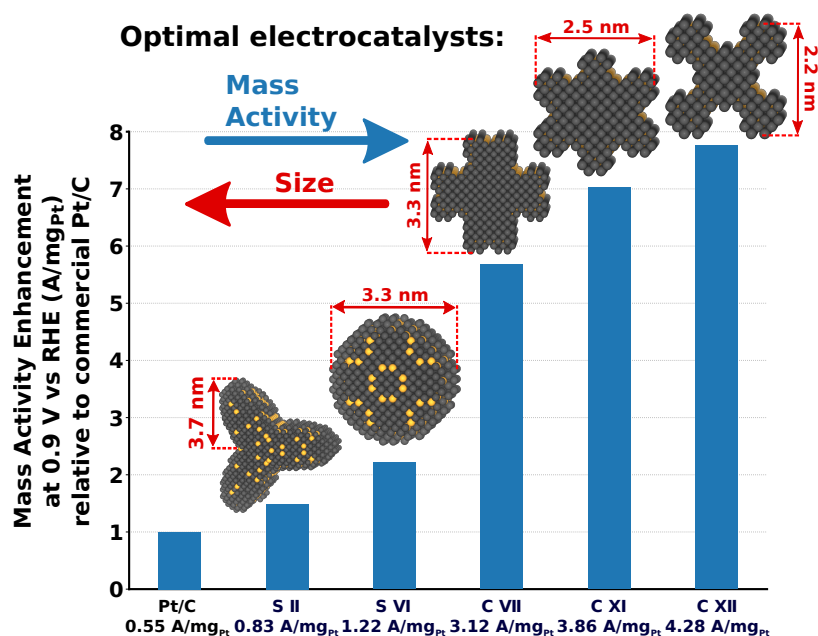
Figure 3.3: Tailored electrocatalysts with high predicted activities. Active sites with $7.5 \leq \overline{CN} \leq 8.3$ are highlighted in yellow. Adapted with permission from Ref. 98. Published by The Royal Society of Chemistry (RSC).

tive steps.

The tailored electrocatalysts have predicted mass activities of up to 4.28 A mg_{Pt}^{-1} (see Figure 3.3), which corresponds to 7.8-fold enhancement over Tanaka commercial Pt/C catalysts.[49] Such high activities originate from numerous active sites tailored at concave kinks of the nanostructure, where local-site structures are close to the volcano-shaped activity peak at generalized coordination $\overline{CN} = 8.1$. Furthermore, we investigate how mass activities change upon the electrocatalyst size. Upon small size changes, the most active nanostructure retains high mass activities above 3.4 A mg_{Pt}^{-1}.

In sum, the high predicted mass activities from this study show that Pt electrocatalysts have great potential to reduce the Pt loading in PEM fuel cells. The chemical synthesis guidelines, which are derived from the size effect studies in this thesis, may foster and support experimental works on pure Pt electrocatalysts.

Individual contributions:

I substantially contributed to the ideas and implementations of the computational electrocatalyst screenings in this study. I combined the Superformula with Particle Swarm Optimization and linked them with our computational model to enable effective electrocatalyst optimization toward highest ORR activities. I authored the manuscript considering insightful prospects and viewpoints on catalysis modeling, synthesis, and characterization provided by the co-authors.

3.4   Oxygen Reduction Activities of Strained Platinum Core-Shell Electrocatalysts Predicted by Machine Learning

Herein, we propose core-shell nanocatalysts with optimal mass activities, which are largely controlled by bimetallic composition, shell thickness, and nanoparticle size. We present a machine learning framework to predict strains with site-specific precision, which are induced by the different lattice constants between core metal and Pt shell. Based on predicted strains, we determine strained generalized coordination numbers $\overline{CN}^*$ to enable mass activity forecasts by our computational model. We investigate fcc core metals Ni, Cu, Pd, Au, and Ag with Pt shell thicknesses of 2-3 and 3-4 monolayers, for which ligand effects are demonstrated to be negligible and the activity enhancements are mainly attributed to strain effects.[39,84,85,89–92] Mass activities predicted by the computational model are shown to be in good agreement with previous experiments on 5±1 nm sized Pt@Au nanoparticles (see Figure 3.4).[80]

Our predictions show that optimal strain degrees, which enhance mass activities,

Figure 3.4: Optimal mass activities predicted for nanoparticles with Pt shells and fcc core metals depending on nanoparticle size and size distribution. Pure Pt nanoparticles and the experimental activity[49] of Tanaka commercial Pt/C are provided as benchmark. For 5 nm sized PtAu, mass activity forecasts are compared with experimental measurements.[80] Reprinted with permission from Ref. 102. Copyright 2020 American Chemical Society.

depend on the nanoparticle size. More precisely, different strain degrees can shift atomic coordinations either closer to the volcano-shaped activity peak at $\overline{CN}^* = 8.1$ or further away from the peak.

Core metals Cu and Ni have smaller lattice constants than Pt, for which highest mass activities of 2.2 A mg_{Pt}^{-1} are predicted for large compressive strain at 1.94 nm size toward small 0.1 nm size distribution. Core metals with larger lattice constant such as Ag and Au induce similar high mass activities by weaker compressive strains at 2.88 nm with small 0.1 nm size distribution. In contrast, Pd cores have small lattice mismatches versus Pt shells, which lead to high mass activities both at 1.94 nm and 2.88 nm size. Thus, we proposed core-shell nanoparticles with various metal compositions, which are up to 4 times more active than Tanaka commercial Pt/C electrocatalysts with 0.55 A mg_{Pt}^{-1}.[49]

Individual contributions:

I substantially contributed to the ideas and implementations of the data analytics approaches in this study. I linked Kernel Ridge Regression with novel features, which capture bimetallic core-shell geometries, to develop effective machine learning models for strain predictions. I integrated machine learning predictions in our computational model to forecast mass activities within short computation times. I authored the manuscript considering valuable aspects and insights provided by the co-authors.

4   Cross-Article Discussion and Conclusions

Electrocatalysis technologies including Power-To-X and PEM fuel cells can help shape the sustainable energy future.[1] Therein, PEM fuel cells are electrochemical devices to provide manifold stationary and portable power solutions. However, one key factor limiting their widespread commercialization are high costs for large Pt loadings, which are required to catalyze the sluggish ORR at the fuel cell cathode. Thus, new ORR catalysts with enhanced mass activities can help reduce Pt loadings and drive PEM fuel cell technologies.

In this thesis, we capitalize on data-driven design to propose new Pt catalysts with enhanced mass activities toward the ORR. We combine DFT results with experimental data on Pt-based ORR catalysts to build a computational model, which predicts ORR activities upon nanostructure geometries. This realizes reduced computation times and the consideration of size distributions in comparison to theoretical predictions solely based on DFT. The predicted mass activities from the computational model are in good agreement with the experimental measurements from *Perez-Alonso et al.*[57] for various nanoparticle sizes. Beyond thitherto available experiments, we predict optimal mass activities at 1.1, 2.07, and 2.87 nm size toward small size distribution near 0.1 nm.

In interdisciplinary collaborations, we accomplished synthesis of the proposed 1.1 nm sized Pt nanoparticles using a ZIF-8 metal-organic framework.[121] Their mass activities of 0.87 ± 0.14 A mg_{Pt}^{-1} coincide with the computational predictions (0.99 A mg_{Pt}^{-1}). The catalysts show similar stabilities relative to commercial Pt/C. Thus, we synthesized 1.1 nm sized Pt nanoparticles by computational design, which double the mass activity at comparable stability of current commercial Pt/C electrocatalysts.

The oberserved theoretical limit, that pure Pt nanocatalysts with sphere-like shapes are limited to ca 2 A mg_{Pt}^{-1} in mass activity,[103] substantiates the high demand for shape and size engineering toward further enhanced mass activities. We presented a computational framework for high-throughput screenings to tailor electrocatalyst shapes and sizes toward highest mass activities. The generalization of the Superfomula provides symmetric nanoshapes, which generate a wide variety of nanostructures. The nanostructures were optimized toward the highest predicted mass activities by Particle Swarm Optimization. The optimized electrocatalysts yield predicted mass activities of up to 4.28 A mg_{Pt}^{-1}, which corresponds to 7.8-fold enhancement over Tanaka commercial Pt/C catalysts. The high activities are attributed to numerous active sites, which are arranged in a side-by-side formation at concave kinks of the nanostructure. The chemical synthesis guidelines provided in this thesis may foster and support upcoming experimental works on tailored electrocatalysts. The

nanostructing of superior active sites in cavities[43] and at concavities[50, 83, 97, 122] is part of ongoing theoretical and experimental catalyst research.

In core-shell nanoparticles, the catalysis takes place on active Pt shells, but cheaper and more abundant metals at the core limit the precious Pt loading. We presented a machine learning framework for strain prediction on core-shell nanoparticles. The machine learning models link KRR with novel features, which capture the bimetallic core-shell geometries. One crucial feature is the PDF, which we adapt to describe the deviation between the bimetallic core-shell configuration and the atomic configuration in pure Pt nanoparticles. Variations of the PDF have been previously applied in KRR machine learning to predict nanostructure properties.[116–119]

Based on machine learning predicted strains, we determine strained generalized coordination numbers $\overline{CN}^*$ to enable mass activity forecasts by our computational model. The predicted mass activities are in good agreement with previous experiments on 5±1 nm sized Pt@Au nanoparticles from *Hu et al.*.[80]

We demonstrate that optimal strain degrees, which enhance mass activities, depend on the nanoparticle size. Large compressive strains on Pt@Cu and Pt@Ni result in optimal mass activities of up to 2.2 A mg_{Pt}^{-1} at 1.94 nm nanoparticle size toward small size distribution around 0.1 nm. Weaker compressive strains on Pt@Ag and Pt@Au induce similar high mass activities at 2.83 nm with small 0.1 nm size distribution. Thus, we propose core-shell nanoparticles with various metal compositions, which are up to 4 times more active than Tanaka commercial Pt/C electrocatalysts with 0.55 A mg_{Pt}^{-1} mass activity.[49]

5   Perspectives

The computational approaches presented in this thesis have not only rendered important contributions to the development of recent new catalysts, but they may also help shape new catalyst technologies in future studies. The peak of the activity-volcano derived in this thesis shows that site-specific activities toward the ORR are limited to the maximum increase of 8-fold activity relative to Pt(111).[103] However, the activity peak may be shifted upwards by breaking the scaling relations between the adsorption energies of ORR intermediates. This is increasingly attracting broad interest in catalyst research.[123–126] Though it might not be a straightforward task, the computational model for mass activity prediction may be adapted to broken scaling relations. It is important to note in this context that predicting mass activities for the ORR in absolute units within feasible computation times, which is achieved by the computational model, is still unique in catalyst literature.

Nanostructured electroctalysts with tailored shapes and sizes have been proposed in this thesis to yield superior mass activities toward the ORR. On the experimental side, Pt-alloy nanocatalysts with stellated shapes[109] and pure Pt nanocatalysts with concave surface shapes[122] have recently been proposed for the ORR. The stellated shapes[109] and the concave surface shapes[122] are similar to the ORR active shapes tailored in this thesis.[98] The precision in nanostructure synthesis on the sub-nanometer scale has been rapidly advancing during the past two decades.[68,127] Therefore, prospects in electrocatalyst synthesis with tailored shapes and sizes, which are proposed in this thesis, will likely increase during the next years.

Finding new material compositions for ORR core-shell nanoparticles has recently been addressed in many experimental and theory studies. Pt core-shell nanoparticles, which include core metals other than fcc, such as Pt@Y[85] and Pt@Ti[87] are promising candidates for high ORR activities. Bimetallic Ti-Au cores on Pt shells have been experimentally shown to improve the mass activity and stability of Pt@Au.[80] Further bimetallic alloy cores in core-shell nanoparticles such as Pt@Pt-Co,[128] Pt@Pd-Au,[77] and Pt-Cu@Pd-Cu[88] have been proposed to yield high ORR activities. The machine learning framework, which is presented in this thesis, may help explore new and more complex core-shell compounds in future studies, for which computational predictions solely based on DFT are expensive and costly in time.

References

[1] Z. W. She, J. Kibsgaard, C. F. Dickens, I. Chorkendorff, J. K. Nørskov, and T. F. Jaramillo, "Combining theory and experiment in electrocatalysis: insights into materials design," *Science*, vol. 355, no. 6321, 2017.

[2] A. A. Peterson and J. K. Nørskov, "Activity descriptors for CO2 electroreduction to methane on transition-metal catalysts," *J. Phys. Chem. Lett.*, vol. 3, no. 2, pp. 251–258, 2012.

[3] Y. Wang, H. Shen, K. J. T. Livi, D. Raciti, H. Zong, J. Gregg, M. Onadeko, Y. Wan, A. Watson, and C. Wang, "Copper nanocubes for CO2 reduction in gas diffusion electrodes," *Nano Lett.*, vol. 19, no. 12, pp. 8461–8468, 2019.

[4] S. A. Nitopi, E. Bertheussen, S. B. Scott, X. Liu, K. Albert, S. Horch, B. Seger, I. E. L. Stephens, K. Chan, J. K. Nørskov, T. F. Jaramillo, and I. Chorkendorff, "Progress and perspectives of electrochemical CO2 reduction on copper in aqueous electrolyte," *Chem. Rev.*, vol. 119, no. 12, pp. 7610–7672, 2018.

[5] Y. Hori, A. Murata, and R. Takahashi, "Formation of hydrocarbons in the electrochemical reduction of carbon dioxide at a copper electrode in aqueous solution," *J. Chem. Soc. Faraday Trans. 1 Phys. Chem. Condens. Phases*, vol. 85, no. 8, pp. 2309–2326, 1989.

[6] D. Raciti, K. J. Livi, and C. Wang, "Highly dense Cu nanowires for low-overpotential CO2 reduction," *Nano Lett.*, vol. 15, no. 10, pp. 6829–6835, 2015.

[7] Y. Li, F. Cui, M. B. Ross, D. Kim, Y. Sun, and P. Yang, "Structure-sensitive CO2 electroreduction to hydrocarbons on ultrathin 5-fold twinned copper nanowires," *Nano Lett.*, vol. 17, no. 2, pp. 1312–1317, 2017.

[8] Z. Zhao, Z. Chen, X. Zhang, and G. Lu, "Generalized surface coordination number as an activity descriptor for CO2 reduction on Cu surfaces," *J. Phys. Chem. C*, vol. 120, no. 49, pp. 28125–28130, 2016.

[9] S. Zhao, R. Jin, and R. Jin, "Opportunities and challenges in CO2 reduction by gold- and silver-based electrocatalysts: from bulk metals to nanoparticles and atomically precise nanoclusters," *ACS Energy Lett.*, vol. 3, no. 2, pp. 452–462, 2018.

[10] A. A. Peterson, F. Abild-Pedersen, F. Studt, J. Rossmeisl, and J. K. Nørskov, "How copper catalyzes the electroreduction of carbon dioxide into hydrocarbon fuels," *Energy Environ. Sci.*, vol. 3, no. 9, pp. 1311–1315, 2010.

[11] F. Calle-Vallejo and M. T. Koper, "Theoretical considerations on the electrore-duction of CO to C2 Species on Cu(100) electrodes," *Angew. Chemie - Int. Ed.*, vol. 52, no. 28, pp. 7282–7285, 2013.

[12] L. Cao, D. Raciti, C. Li, K. J. Livi, P. F. Rottmann, K. J. Hemker, T. Mueller, and C. Wang, "Mechanistic insights for low-overpotential electroreduction of CO2 to CO on copper nanowires," *ACS Catal.*, vol. 7, no. 12, pp. 8578–8587, 2017.

[13] Y. Jiao, Y. Zheng, M. Jaroniec, and S. Z. Qiao, "Design of electrocatalysts for oxygen- and hydrogen-involving energy conversion reactions," *Chem. Soc. Rev.*, vol. 44, no. 8, pp. 2060–2086, 2015.

[14] H. Deng, C. Zhang, Y. Xie, T. Tumlin, L. Giri, S. P. Karna, and J. Lin, "A highly active and stable IrOx/SrIrO3 catalyst for the oxygen evolution reac-tion," *J. Mater. Chem. A*, vol. 4, no. 6303, pp. 6824–6830, 2016.

[15] J. Kibsgaard and I. Chorkendorff, "Considerations for the scaling-up of water splitting catalysts," *Nat. Energy*, vol. 4, no. 6, pp. 430–433, 2019.

[16] L. A. King, M. K. Hubert, C. Capuano, J. Manco, N. Danilovic, E. Valle, T. R. Hellstern, K. Ayers, and T. F. Jaramillo, "A non-precious metal hydro-gen catalyst in a commercial polymer electrolyte membrane electrolyser," *Nat. Nanotechnol.*, vol. 14, no. 11, pp. 1071–1074, 2019.

[17] "Hydrogen to the rescue," *Nat. Mater.*, vol. 17, no. 7, p. 565, 2018.

[18] D. T. Whipple and P. J. Kenis, "Prospects of CO2 utilization via direct het-erogeneous electrochemical reduction," *J. Phys. Chem. Lett.*, vol. 1, no. 24, pp. 3451–3458, 2010.

[19] C. W. Li, J. Ciston, and M. W. Kanan, "Electroreduction of carbon monoxide to liquid fuel on oxide-derived nanocrystalline copper," *Nature*, vol. 508, no. 7497, pp. 504–507, 2014.

[20] W. Zhang, Y. Hu, L. Ma, G. Zhu, Y. Wang, X. Xue, R. Chen, S. Yang, and Z. Jin, "Progress and perspective of electrocatalytic CO2 reduction for renew-able carbonaceous fuels and chemicals," *Adv. Sci.*, vol. 5, no. 1, p. 1700275, 2018.

[21] D. Spreitzer and J. Schenk, "Reduction of iron oxides with hydrogen - a review," *Steel Res. Int.*, vol. 90, no. 10, 2019.

[22] S. Niaz, T. Manzoor, and A. H. Pandith, "Hydrogen storage: materials, methods and perspectives," *Renew. Sustain. Energy Rev.*, vol. 50, pp. 457–469, 2015.

[23] H. A. Gasteiger and N. M. Marković, "Just a Dream or Future Reality?," *Science*, vol. 324, no. 5923, pp. 48–49, 2009.

[24] W. J. Durand, A. A. Peterson, F. Studt, F. Abild-Pedersen, and J. K. Nørskov, "Structure effects on the energetics of the electrochemical reduction of CO2 by copper surfaces," *Surf. Sci.*, vol. 605, no. 15-16, pp. 1354–1359, 2011.

[25] X. Nie, M. R. Esopi, M. J. Janik, and A. Asthagiri, "Selectivity of CO2 reduction on copper electrodes: the role of the kinetics of elementary steps," *Angew. Chemie - Int. Ed.*, vol. 52, no. 9, pp. 2459–2462, 2013.

[26] A. Bagger, W. Ju, A. S. Varela, P. Strasser, and J. Rossmeisl, "Electrochemical CO2 reduction: a classification problem," *ChemPhysChem*, vol. 18, no. 22, pp. 3266–3273, 2017.

[27] O. Z. Sharaf and M. F. Orhan, "An overview of fuel cell technology: Fundamentals and applications," *Renew. Sustain. Energy Rev.*, vol. 32, pp. 810–853, 2014.

[28] T. Wilberforce, A. Alaswad, A. Palumbo, M. Dassisti, and A. G. Olabi, "Advances in stationary and portable fuel cell applications," *Int. J. Hydrogen Energy*, vol. 41, no. 37, pp. 16509–16522, 2016.

[29] M. K. Debe, "Electrocatalyst approaches and challenges for automotive fuel cells," *Nature*, vol. 486, no. 7401, pp. 43–51, 2012.

[30] H. A. Gasteiger, S. S. Kocha, B. Sompalli, and F. T. Wagner, "Activity benchmarks and requirements for Pt, Pt-alloy, and non-Pt oxygen reduction catalysts for PEMFCs," *Appl. Catal. B Environ.*, vol. 56, no. 1-2, pp. 9–35, 2005.

[31] J. Wu, X. Z. Yuan, J. J. Martin, H. Wang, J. Zhang, J. Shen, S. Wu, and W. Merida, "A review of PEM fuel cell durability: degradation mechanisms and mitigation strategies," *J. Power Sources*, vol. 184, no. 1, pp. 104–119, 2008.

[32] L. Dubau, L. Castanheira, F. Maillard, M. Chatenet, O. Lottin, G. Maranzana, J. Dillet, A. Lamibrac, J. C. Perrin, E. Moukheiber, A. Elkaddouri, G. De Moor, C. Bas, L. Flandin, and N. Caqué, "A review of PEM fuel cell durability: materials degradation, local heterogeneities of aging and possible mitigation strategies," *Wiley Interdiscip. Rev. Energy Environ.*, vol. 3, no. 6, pp. 540–560, 2014.

[33] I. E. L. Stephens, J. Rossmeisl, and I. Chorkendorff, "Toward sustainable fuel cells," *Science*, vol. 354, no. 6318, pp. 1378–1379, 2016.

[34] "Fuel Cell Technical Team Roadmap." `https://www.energy.gov/sites/prod/files/2014/02/f8/fctt_roadmap_june2013.pdf` (online 2013; accessed 09/28/2020).

[35] B. Cai, S. Henning, J. Herranz, T. J. Schmidt, and A. Eychmüller, "Nanostructuring noble metals as unsupported electrocatalysts for polymer electrolyte fuel cells," *Advanced Energy Materials*, vol. 7, no. 23, pp. 1–16, 2017.

[36] J. K. Nørskov, J. Rossmeisl, A. Logadottir, L. Lindqvist, J. R. Kitchin, T. Bligaard, and H. Jónsson, "Origin of the overpotential for oxygen reduction at a fuel-cell cathode," *J. Phys. Chem. B*, vol. 108, no. 46, pp. 17886–17892, 2004.

[37] V. Stamenkovic, B. S. Mun, K. J. Mayrhofer, P. N. Ross, N. M. Markovic, J. Rossmeisl, J. Greeley, and J. K. Nørskov, "Changing the activity of electrocatalysts for oxygen reduction by tuning the surface electronic structure," *Angew. Chemie Int. Ed.*, vol. 45, no. 18, pp. 2897–2901, 2006.

[38] J. Greeley, I. E. L. Stephens, A. S. Bondarenko, T. P. Johansson, H. A. Hansen, T. F. Jaramillo, J. Rossmeisl, I. Chorkendorff, and J. K. Nørskov, "Alloys of platinum and early transition metals as oxygen reduction electrocatalysts," *Nat. Chem.*, vol. 1, no. 7, pp. 552–556, 2009.

[39] I. E. L. Stephens, A. S. Bondarenko, F. J. Perez-Alonso, F. Calle-Vallejo, L. Bech, T. P. Johansson, A. K. Jepsen, R. Frydendal, B. P. Knudsen, J. Rossmeisl, and I. Chorkendorff, "Tuning the activity of Pt(111) for oxygen electroreduction by subsurface alloying," *J. Am. Chem. Soc.*, vol. 133, no. 14, pp. 5485–5491, 2011.

[40] I. E. L. Stephens, A. S. Bondarenko, U. Grønbjerg, J. Rossmeisl, and I. Chorkendorff, "Understanding the electrocatalysis of oxygen reduction on platinum and its alloys," *Energy Environ. Sci.*, vol. 5, no. 5, pp. 6744–6762, 2012.

[41] V. Čolić and A. S. Bandarenka, "Pt alloy electrocatalysts for the oxygen reduction reaction: from model surfaces to nanostructured systems," *ACS Catal.*, vol. 6, no. 8, pp. 5378–5385, 2016.

[42] M. Escudero-Escribano, P. Malacrida, M. H. Hansen, U. G. Vej-Hansen, A. Velázquez-Palenzuela, V. Tripkovic, J. Schiøtz, J. Rossmeisl, I. E. L. Stephens, and I. Chorkendorff, "Tuning the activity of Pt alloy electrocatalysts

by means of the lanthanide contraction," *Science*, vol. 352, no. 6281, pp. 73–76, 2016.

[43] F. Calle-Vallejo, J. Tymoczko, V. Colic, Q. H. Vu, M. D. Pohl, K. Morgenstern, D. Loffreda, P. Sautet, W. Schuhmann, and A. S. Bandarenka, "Finding optimal surface sites on heterogeneous catalysts by counting nearest neighbors," *Science*, vol. 350, no. 6257, pp. 185–189, 2015.

[44] B. Garlyyev, S. Xue, M. D. Pohl, D. Reinisch, and A. S. Bandarenka, "Oxygen electroreduction at high-index Pt electrodes in alkaline electrolytes: a decisive role of the alkali metal cations," *ACS Omega*, vol. 3, no. 11, pp. 15325–15331, 2018.

[45] Z. Duan and G. Wang, "A first principles study of oxygen reduction reaction on a Pt(111) surface modified by a subsurface transition metal M (M = Ni, Co, or Fe)," *Phys. Chem. Chem. Phys.*, vol. 13, no. 45, pp. 20178–20187, 2011.

[46] Z. Duan and G. Wang, "Comparison of reaction energetics for oxygen reduction reactions on Pt(100), Pt(111), Pt/Ni(100), and Pt/Ni(111) surfaces: a first-principles study," *J. Phys. Chem. C*, vol. 117, no. 12, pp. 6284–6292, 2013.

[47] P. Strasser, M. Gliech, S. Kuehl, and T. Moeller, "Electrochemical processes on solid shaped nanoparticles with defined facets," *Chem. Soc. Rev.*, vol. 47, no. 3, pp. 715–735, 2018.

[48] J. Fichtner, B. Garlyyev, S. Watzele, H. A. El-Sayed, J. N. Schwämmlein, W. J. Li, F. M. Maillard, L. Dubau, J. Michalička, J. M. Macak, A. Holleitner, and A. S. Bandarenka, "Top-down synthesis of nanostructured platinum-lanthanide alloy oxygen reduction reaction catalysts: Pt x Pr/C as an example," *ACS Appl. Mater. Interfaces*, vol. 11, no. 5, pp. 5129–5135, 2019.

[49] A. Orfanidi, P. Madkikar, H. A. El-Sayed, G. S. Harzer, T. Kratky, and H. A. Gasteiger, "The key to high performance low Pt loaded electrodes," *J. Electrochem. Soc.*, vol. 164, no. 4, pp. F418–F426, 2017.

[50] F. Calle-Vallejo, M. D. Pohl, D. Reinisch, D. Loffreda, P. Sautet, and A. S. Bandarenka, "Why conclusions from platinum model surfaces do not necessarily lead to enhanced nanoparticle catalysts for the oxygen reduction reaction," *Chem. Sci.*, vol. 8, no. 3, pp. 2283–2289, 2017.

[51] M. D. Macia, J. M. Campina, E. Herrero, and J. M. Feliu, "On the kinetics of oxygen reduction on platinum stepped surfaces in acidic media," *J. Electroanal. Chem.*, vol. 564, no. 1-2, pp. 141–150, 2004.

[52] A. Kuzume, E. Herrero, and J. M. Feliu, "Oxygen reduction on stepped platinum surfaces in acidic media," *J. Electroanal. Chem.*, vol. 599, no. 2, pp. 333–343, 2007.

[53] A. Hitotsuyanagi, M. Nakamura, and N. Hoshi, "Structural effects on the activity for the oxygen reduction reaction on n(111)–(100) series of Pt: correlation with the oxide film formation," *Electrochim. Acta*, vol. 82, pp. 512–516, 2012.

[54] A. S. Bandarenka, H. A. Hansen, J. Rossmeisl, and I. E. L. Stephens, "Elucidating the activity of stepped Pt single crystals for oxygen reduction," *Phys. Chem. Chem. Phys.*, vol. 16, no. 27, pp. 13625–13629, 2014.

[55] J. Kibsgaard, Y. Gorlin, Z. Chen, and T. F. Jaramillo, "Meso-structured platinum thin films: Active and stable electrocatalysts for the oxygen reduction reaction," *J. Am. Chem. Soc.*, vol. 134, no. 18, pp. 7758–7765, 2012.

[56] M. Shao, A. Peles, and K. Shoemaker, "Electrocatalysis on platinum nanoparticles: particle size effect on oxygen reduction reaction activity," *Nano Lett.*, vol. 11, no. 9, pp. 3714–3719, 2011.

[57] F. J. Perez-Alonso, D. N. McCarthy, A. Nierhoff, P. Hernandez-Fernandez, C. Strebel, I. E. L. Stephens, J. H. Nielsen, and I. Chorkendorff, "The effect of size on the oxygen electroreduction activity of mass-selected platinum nanoparticles," *Angew. Chemie - Int. Ed.*, vol. 51, no. 19, pp. 4641–4643, 2012.

[58] G. A. Tritsaris, J. Greeley, J. Rossmeisl, and J. K. Nørskov, "Atomic-scale modeling of particle size effects for the oxygen reduction reaction on Pt," *Catal. Letters*, vol. 141, no. 7, pp. 909–913, 2011.

[59] P. Strasser, "Catalysts by platonic design," *Science*, vol. 349, no. 6246, pp. 379–380, 2015.

[60] C. Kim, F. Dionigi, V. Beermann, X. Wang, T. Möller, and P. Strasser, "Alloy nanocatalysts for the electrochemical oxygen reduction (ORR) and the direct electrochemical carbon dioxide reduction reaction (CO2RR)," *Adv. Mater.*, vol. 1805617, pp. 1–19, 2018.

[61] V. R. Stamenkovic, B. Fowler, B. S. Mun, G. Wang, P. N. Ross, C. A. Lucas, and N. M. Markovic, "Improved oxygen reduction activity on Pt3Ni(111) via increased surface site availability," *Science*, vol. 315, no. 5811, pp. 493–497, 2007.

[62] C. Cui, L. Gan, H. H. Li, S. H. Yu, M. Heggen, and P. Strasser, "Octahedral PtNi nanoparticle catalysts: exceptional oxygen reduction activity by tuning

the alloy particle surface composition," *Nano Lett.*, vol. 12, no. 11, pp. 5885–5889, 2012.

[63] S. I. Choi, S. Xie, M. Shao, J. H. Odell, N. Lu, H. C. Peng, L. Protsailo, S. Guerrero, J. Park, X. Xia, J. Wang, M. J. Kim, and Y. Xia, "Synthesis and characterization of 9 nm Pt-Ni octahedra with a record high activity of 3.3 A/mgPt for the oxygen reduction reaction," *Nano Lett.*, vol. 13, no. 7, pp. 3420–3425, 2013.

[64] C. Chen, Y. Kang, Z. Huo, Z. Zhu, W. Huang, H. L. Xin, J. D. Snyder, D. Li, J. A. Herron, M. Mavrikakis, M. Chi, K. L. More, Y. Li, N. M. Markovic, G. A. Somorjai, P. Yang, and V. R. Stamenkovic, "Highly crystalline multimetallic nanoframes with three-dimensional electrocatalytic surfaces," *Science*, vol. 343, no. 6177, pp. 1339–1343, 2014.

[65] V. Beermann, M. Gocyla, E. Willinger, S. Rudi, M. Heggen, R. E. Dunin-Borkowski, M. G. Willinger, and P. Strasser, "Rh-Doped Pt-Ni octahedral nanoparticles: understanding the correlation between elemental distribution, oxygen reduction reaction, and shape stability," *Nano Lett.*, vol. 16, no. 3, pp. 1719–1725, 2016.

[66] Q. Jia, Z. Zhao, L. Cao, J. Li, S. Ghoshal, V. Davies, E. Stavitski, K. Attenkofer, Z. Liu, M. Li, X. Duan, S. Mukerjee, T. Mueller, and Y. Huang, "Roles of mo surface dopants in enhancing the orr performance of octahedral ptni nanoparticles," *Nano Letters*, vol. 18, no. 2, pp. 798–804, 2018.

[67] J. Lim, H. Shin, M. Kim, H. Lee, K. S. Lee, Y. Kwon, D. Song, S. Oh, H. Kim, and E. Cho, "Ga-doped Pt-Ni octahedral nanoparticles as a highly active and durable electrocatalyst for oxygen reduction reaction," *Nano Lett.*, vol. 18, no. 4, pp. 2450–2458, 2018.

[68] A. Mahata, A. S. Nair, and B. Pathak, "Recent advancements of Pt-nanostructure based electrocatalysts for oxygen reduction reaction," *Catal. Sci. Technol.*, vol. 9, pp. 4835–4863, 2019.

[69] F. Calle-Vallejo, J. I. Martínez, J. M. García-Lastra, P. Sautet, and D. Loffreda, "Fast prediction of adsorption properties for platinum nanocatalysts with generalized coordination numbers," *Angew. Chemie - Int. Ed.*, vol. 53, no. 32, pp. 8316–8319, 2014.

[70] F. Calle-Vallejo and A. S. Bandarenka, "Enabling generalized coordination numbers to describe strain effects," *ChemSusChem*, vol. 11, no. 11, pp. 1824–1828, 2018.

[71] G. G. Asara, L. O. Paz-Borbón, and F. Baletto, ""Get in touch and keep in contact": interface effect on the oxygen reduction reaction (ORR) activity for supported PtNi nanoparticles," *ACS Catal.*, vol. 6, no. 7, pp. 4388–4393, 2016.

[72] B. Hammer and J. K. Nørskov, "Theoretical surface science and catalysis - calculations and concepts," *Adv. Catal.*, vol. 45, pp. 71–129, 2000.

[73] V. R. Stamenkovic, B. S. Mun, M. Arenz, K. J. Mayrhofer, C. A. Lucas, G. Wang, P. N. Ross, and N. M. Markovic, "Trends in electrocatalysis on extended and nanoscale Pt-bimetallic alloy surfaces," *Nat. Mater.*, vol. 6, no. 3, pp. 241–247, 2007.

[74] H. Xin, A. Holewinski, and S. Linic, "Predictive structure reactivity models for rapid screening of pt-based multimetallic electrocatalysts for the oxygen reduction reaction," *ACS Catal.*, vol. 2, no. 1, pp. 12–16, 2012.

[75] X. Ma and H. Xin, "Orbitalwise coordination Number for predicting adsorption properties of metal nanocatalysts," *Phys. Rev. Lett.*, vol. 118, no. 3, pp. 1–5, 2017.

[76] D. Wu, C. Dong, H. Zhan, and X. W. Du, "Bond-energy-integrated descriptor for oxygen electrocatalysis of transition metal oxides," *J. Phys. Chem. Lett.*, vol. 9, no. 12, pp. 3387–3391, 2018.

[77] L. Zhang, R. Iyyamperumal, D. F. Yancey, R. M. Crooks, and G. Henkelman, "Design of Pt-shell nanoparticles with alloy cores for the oxygen reduction reaction," *ACS Nano*, vol. 7, no. 10, pp. 9168–9172, 2013.

[78] T. S. Choksi, L. T. Roling, V. Streibel, and F. Abild-Pedersen, "Predicting adsorption properties of catalytic descriptors on bimetallic nanoalloys with site-specific precision," *The Journal of Physical Chemistry Letters*, vol. 10, no. 8, pp. 1852–1859, 2019.

[79] L. Wang, A. Holewinski, and C. Wang, "Prospects of Platinum-Based Nanostructures for the Electrocatalytic Reduction of Oxygen," *ACS Catal.*, vol. 8, no. 10, pp. 9388–9398, 2018.

[80] J. Hu, L. Wu, K. A. Kuttiyiel, K. R. Goodman, C. Zhang, Y. Zhu, M. B. Vukmirovic, M. G. White, K. Sasaki, and R. R. Adzic, "Increasing stability and activity of core-shell catalysts by preferential segregation of oxide on edges and vertexes: oxygen reduction on Ti-Au@Pt/C," *J. Am. Chem. Soc.*, vol. 138, no. 29, pp. 9294–9300, 2016.

[81] S. E. Temmel, E. Fabbri, D. Pergolesi, T. Lippert, and T. J. Schmidt, "Investigating the role of strain toward the oxygen reduction activity on model thin film Pt catalysts," *ACS Catal.*, vol. 6, no. 11, pp. 7566–7576, 2016.

[82] Y. J. Deng, V. Tripkovic, J. Rossmeisl, and M. Arenz, "Oxygen reduction reaction on Pt overlayers deposited onto a gold film: ligand, strain, and ensemble effect," *ACS Catal.*, vol. 6, no. 2, pp. 671–676, 2016.

[83] R. Chattot, O. Le Bacq, V. Beermann, S. Kühl, J. Herranz, S. Henning, L. Kühn, T. Asset, L. Guétaz, G. Renou, J. Drnec, P. Bordet, A. Pasturel, A. Eychmüller, T. J. Schmidt, P. Strasser, L. Dubau, and F. Maillard, "Surface distortion as a unifying concept and descriptor in oxygen reduction reaction electrocatalysis," *Nat. Mater.*, vol. 17, no. 9, pp. 827–833, 2018.

[84] P. Strasser, S. Koh, T. Anniyev, J. Greeley, K. More, C. Yu, Z. Liu, S. Kaya, D. Nordlund, H. Ogasawara, M. F. Toney, and A. Nilsson, "Lattice-strain control of the activity in dealloyed core-shell fuel cell catalysts," *Nat. Chem.*, vol. 2, no. 6, pp. 454–460, 2010.

[85] P. Hernandez-Fernandez, F. Masini, D. N. McCarthy, C. E. Strebel, D. Friebel, D. Deiana, P. Malacrida, A. Nierhoff, A. Bodin, A. M. Wise, J. H. Nielsen, T. W. Hansen, A. Nilsson, I. E. Stephens, and I. Chorkendorff, "Mass-selected nanoparticles of PtxY as model catalysts for oxygen electroreduction," *Nat. Chem.*, vol. 6, no. 8, pp. 732–738, 2014.

[86] J. Shin, J.-H. Choi, P.-R. Cha, S. K. Kim, I. Kim, S.-C. Lee, and D. S. Jeong, "Catalytic activity for oxygen reduction reaction on platinum-based core–shell nanoparticles: all-electron density functional theory," *Nanoscale*, vol. 7, no. 38, pp. 15830–15839, 2015.

[87] A. S. Nair and B. Pathak, "Computational screening for ORR activity of 3d transition metal based M@Pt core–shell clusters," *J. Phys. Chem. C*, vol. 123, pp. 3634–3644, 2019.

[88] J. T. L. Gamler, A. Leonardi, H. M. Ashberry, N. N. Daanen, Y. Losovyj, R. R. Unocic, M. Engel, and S. E. Skrabalak, "Achieving highly durable random alloy nanocatalysts through intermetallic cores," *ACS Nano*, p. Accepted for publication, 2019.

[89] A. Schlapka, M. Lischka, A. Groß, U. Käsberger, and P. Jakob, "Surface strain versus substrate interaction in heteroepitaxial metal layers: Pt on Ru(0001)," *Phys. Rev. Lett.*, vol. 91, no. 1, p. 016101, 2003.

[90] M. Lischka, C. Mosch, and A. Groß, "Tuning catalytic properties of bimetallic surfaces: oxygen adsorption on pseudomorphic Pt/Ru overlayers," *Electrochim. Acta*, vol. 52, no. 6, pp. 2219–2228, 2007.

[91] I. A. Pašti, E. Fako, A. S. Dobrota, N. López, N. V. Skorodumova, and S. V. Mentus, "Atomically thin metal films on foreign substrates: from lattice mismatch to electrocatalytic activity," *ACS Catal.*, vol. 9, no. 4, pp. 3467–3481, 2019.

[92] R. Yang, J. Leisch, P. Strasser, and M. F. Toney, "Structure of dealloyed PtCu3 thin films and catalytic activity for oxygen reduction," *Chem. Mater.*, vol. 22, no. 16, pp. 4712–4720, 2010.

[93] F. Calle-Vallejo, D. Loffreda, M. T. M. Koper, and P. Sautet, "Introducing structural sensitivity into adsorption-energy scaling relations by means of coordination numbers," *Nat. Chem.*, vol. 7, no. 5, pp. 403–410, 2015.

[94] H. Li, Y. Li, M. T. Koper, and F. Calle-Vallejo, "Bond-making and breaking between carbon, nitrogen, and oxygen in electrocatalysis," *J. Am. Chem. Soc.*, vol. 136, no. 44, pp. 15694–15701, 2014.

[95] J. Kleis, J. Greeley, N. A. Romero, V. A. Morozov, H. Falsig, A. H. Larsen, J. Lu, J. J. Mortensen, M. Dułak, K. S. Thygesen, J. K. Nørskov, and K. W. Jacobsen, "Finite size effects in chemical bonding: From small clusters to solids," *Catal. Letters*, vol. 141, no. 8, pp. 1067–1071, 2011.

[96] G. Mpourmpakis, A. N. Andriotis, and D. G. Vlachos, "Identification of descriptors for the CO interaction with metal nanoparticles," *Nano Lett.*, vol. 10, no. 3, pp. 1041–1045, 2010.

[97] K. Rossi, G. G. Asara, and F. Baletto, "A genomic characterisation of monometallic nanoparticles," *Phys. Chem. Chem. Phys.*, vol. 21, no. 9, pp. 4888–4898, 2018.

[98] M. Rück, A. S. Bandarenka, F. Calle-Vallejo, and A. Gagliardi, "Fast identification of optimal pure platinum nanoparticle shapes and sizes for efficient oxygen electroreduction," *Nanoscale Adv.*, vol. 1, no. 8, pp. 2901–2909, 2019.

[99] F. Calle-Vallejo, M. D. Pohl, and A. S. Bandarenka, "Quantitative coordination-activity relations for the design of enhanced Pt catalysts for CO electrooxidation," *ACS Catal.*, vol. 7, no. 7, pp. 4355–4359, 2017.

[100] M. Jørgensen and H. Grönbeck, "Scaling relations and kinetic monte carlo simulations to bridge the materials gap in heterogeneous catalysis," *ACS Catal.*, vol. 7, no. 8, pp. 5054–5061, 2017.

[101] B. Garlyyev, K. Kratzl, M. Rück, J. Michalička, J. Fichtner, J. Macak, T. Kratky, S. Günther, M. Cokoja, A. Bandarenka, A. Gagliardi, and R. Fischer, "Optimizing the size of platinum nanoparticles for enhanced oxygen electro-reduction mass activity," *Angew. Chemie Int. Ed.*, vol. 58, no. 28, pp. 9596–9600, 2019.

[102] M. Rück, B. Garlyyev, F. Mayr, A. S. Bandarenka, and A. Gagliardi, "Oxygen reduction activities of strained platinum core-shell electrocatalysts predicted by machine learning," *J. Phys. Chem. Lett.*, vol. 11, no. 5, pp. 1773–1780, 2020.

[103] M. Rück, A. Bandarenka, F. Calle-Vallejo, and A. Gagliardi, "Oxygen reduction reaction: rapid prediction of mass activity of unstrained nanostructured platinum electrocatalysts," *J. Phys. Chem. Lett.*, vol. 9, no. 15, pp. 4463–4468, 2018.

[104] F. Viñes, J. R. B. Gomes, and F. Illas, "Understanding the reactivity of metallic nanoparticles: beyond the extended surface model for catalysis," *Chem. Soc. Rev.*, vol. 43, no. 14, pp. 4922–4939, 2014.

[105] M. D. Pohl, V. Colic, D. Scieszka, and A. S. Bandarenka, "Elucidation of adsorption processes at the surface of Pt(331) model electrocatalysts in acidic aqueous media," *Phys. Chem. Chem. Phys.*, vol. 18, no. 16, pp. 10792–10799, 2016.

[106] J. Gielis, "A generic geometric transformation that unifies a wide range of natural and abstract shapes," *Am. J. Bot.*, vol. 90, no. 3, pp. 333–338, 2003.

[107] S. Huclova, D. Erni, and J. Fröhlich, "Modelling effective dielectric properties of materials containing diverse types of biological cells," *J. Phys. D. Appl. Phys.*, vol. 43, no. 36, p. 365405, 2010.

[108] C. Forestiere, Y. He, R. Wang, R. M. Kirby, and L. Dal Negro, "Inverse design of metal nanoparticles' morphology," *ACS Photonics*, vol. 3, no. 1, pp. 68–78, 2016.

[109] H. Liu, F. Ye, Q. Yao, H. Cao, J. Xie, J. Y. Lee, and J. Yang, "Stellated Ag-Pt bimetallic nanoparticles: An effective platform for catalytic activity tuning," *Sci. Rep.*, vol. 4, p. 3969, 2014.

[110] M. K. Baek, J. B. Park, and K. Y. Lee, "An improved attractive and repulsive particle swarm optimization for nonconvex economic dispatch problems," *IFAC-PapersOnLine*, vol. 49, no. 27, pp. 284–289, 2016.

[111] K. W. Jacobsen, P. Stoltze, and J. K. Nørskov, "A semi-empirical effective medium theory for metals and alloys," *Surf. Sci.*, vol. 366, pp. 394–402, 1996.

[112] F. Pedregosa, G. Varoquaux, A. Gramfort, V. Michel, B. Thirion, O. Grisel, M. Blondel, P. Prettenhofer, R. Weiss, V. Dubourg, J. Vanderplas, A. Passos, D. Cournapeau, M. Brucher, M. Perrot, and É. Duchesnay, "Scikit-learn: machine learning in python," *J. Mach. Learn. Res.*, vol. 12, pp. 2825–2830, nov 2011.

[113] C. M. Bishop, *Pattern Recognition and Machine Learning.* Springer Sci. Media, 2006.

[114] L. M. Ghiringhelli, J. Vybiral, E. Ahmetcik, R. Ouyang, S. V. Levchenko, C. Draxl, and M. Scheffler, "Learning physical descriptors for materials science by compressed sensing," *New J. Phys.*, vol. 19, no. 2, p. 023017, 2017.

[115] A. R. Oganov and M. Valle, "How to quantify energy landscapes of solids," *J. Chem. Phys.*, vol. 130, no. 10, 2009.

[116] K. T. Schütt, H. Glawe, F. Brockherde, A. Sanna, K. R. Müller, and E. K. Gross, "How to represent crystal structures for machine learning: Towards fast prediction of electronic properties," *Phys. Rev. B - Condens. Matter Mater. Phys.*, vol. 89, no. 20, pp. 1–5, 2014.

[117] V. Botu and R. Ramprasad, "Adaptive machine learning framework to accelerate ab initio molecular dynamics," *Int. J. Quantum Chem.*, vol. 115, no. 16, pp. 1074–1083, 2015.

[118] A. Seko, H. Hayashi, K. Nakayama, A. Takahashi, and I. Tanaka, "Representation of compounds for machine-learning prediction of physical properties," *Phys. Rev. B*, vol. 95, no. 14, pp. 1–11, 2017.

[119] J. C. Stanley, F. Mayr, and A. Gagliardi, "Machine learning stability and bandgaps of lead-free perovskites for photovoltaics," *Adv. Theory Simulations*, vol. 3, no. 1, p. 1900178, 2020.

[120] A. H. L. Jacobsen, J. J. Mortensen, J. Blomqvist, I. E. Castelli, R. Christensen, M. Dułak, J. Friis, M. N. Groves, B. Hammer, C. Hargus, E. D. Hermes, P. C. Jennings, and P. Bjer, "The atomic simulation environment - a python library

for working with atoms," *J. Phys. Condens. Matter*, vol. 29, no. 27, pp. 273002–273031, 2017.

[121] K. Kratzl, T. Kratky, S. Günther, O. Tomanec, R. Zbořil, J. Michalička, J. M. Macak, M. Cokoja, and R. A. Fischer, "Generation and stabilization of small platinum clusters Pt12±x inside a metal-organic framework," *J. Am. Chem. Soc.*, vol. 141, no. 35, pp. 13962–13969, 2019.

[122] J. Fichtner, S. Watzele, B. Garlyyev, R. M. Kluge, F. Haimerl, H. A. El-Sayed, W.-J. Li, F. M. Maillard, L. Dubau, R. Chattot, J. Michalička, J. M. Macak, W. Wang, D. Wang, T. Gigl, C. Hugenschmidt, and A. S. Bandarenka, "Tailoring the oxygen reduction activity of Pt nanoparticles through surface defects: a simple top-down approach," *ACS Catal.*, vol. 10, no. 5, pp. 3131–3142, 2020.

[123] A. Khorshidi, J. Violet, J. Hashemi, and A. A. Peterson, "How strain can break the scaling relations of catalysis," *Nat. Catal.*, vol. 1, no. April, pp. 263–268, 2018.

[124] Z.-F. Huang, J. Song, S. Dou, X. Li, J. Wang, and X. Wang, "Strategies to break the scaling relation toward enhanced oxygen electrocatalysis," *Matter*, vol. 1, no. 6, pp. 1494–1518, 2019.

[125] N. Govindarajan, M. T. Koper, E. J. Meijer, and F. Calle-Vallejo, "Outlining the scaling-based and scaling-free optimization of electrocatalysts," *ACS Catal.*, vol. 9, no. 5, pp. 4218–4225, 2019.

[126] J. Pérez-Ramírez and N. López, "Strategies to break linear scaling relationships," *Nat. Catal.*, vol. 2, no. 11, pp. 971–976, 2019.

[127] B. Garlyyev, J. Fichtner, O. Piqué, O. Schneider, A. S. Bandarenka, and F. Calle-Vallejo, "Revealing the nature of active sites in electrocatalysis," *Chem. Sci.*, vol. 10, pp. 8060–8075, 2019.

[128] D. Wang, H. L. Xin, R. Hovden, H. Wang, Y. Yu, D. A. Muller, F. J. Disalvo, and H. D. Abruña, "Structurally ordered intermetallic platinum-cobalt core-shell nanoparticles with enhanced activity and stability as oxygen reduction electrocatalysts," *Nat. Mater.*, vol. 12, no. 1, pp. 81–87, 2013.